



Optical constants of polycrystalline Ni from 0.06 to 6.0 eV at 300 K

Farzin Abadizaman¹ and Stefan Zollner^{1,2,a)}

¹Department of Physics, New Mexico State University, P.O. Box 30001, Las Cruces, New Mexico 88003

²Fyzikální ústav AV ČR, v.v.i., Sekce optiky, Na Slovance 2, CZ-18221 Praha 8, Czech Republic

(Received 5 July 2019; accepted 14 October 2019; published 1 November 2019)

Using spectroscopic ellipsometry from 0.06 to 6.0 eV at room temperature, the authors determined the optical constants (complex dielectric function, refractive index, and optical conductivity) of bulk cold-rolled polycrystalline Ni. To reduce the thickness of surface overlayers, the sample was heated in ultrahigh vacuum at 750 K for 6 h and then kept in vacuum during measurements. The authors analyze the optical constants using three alternative but mutually exclusive methods: they write the dielectric function as a multiband sum or product of Drude and Lorentz oscillators or with a Drude model with a frequency-dependent scattering rate and plasma frequency. Below 1 eV, they find significant contributions from both d-intraband transitions and free carriers. © 2019 Author(s). All article content, except where otherwise noted, is licensed under a Creative Commons Attribution (CC BY) license (<http://creativecommons.org/licenses/by/4.0/>). <https://doi.org/10.1116/1.5118841>

I. INTRODUCTION

Determining the complex dielectric function (DF) of bulk metals^{1–3} is difficult, since one needs to minimize overlayers and surface roughness. For example, an Ni surface in air can be covered with a 50 Å thick film of water (or an adsorbed layer with similar optical constants), which is removable by annealing.⁴ It is easier to achieve smooth surfaces of semiconductors than of metals. Clean metal surfaces are best prepared in ultrahigh vacuum (UHV). Ellipsometry measurements should then be performed in UHV without breaking vacuum to maintain a clean surface. This requires window corrections, since vacuum chamber windows disturb the polarization of the incident and reflected light beams.^{5,6}

As early as 1969, Shiga and Pells⁷ overcame these difficulties and measured the optical absorption of annealed polycrystalline bulk Ni from 0.5 to 6.0 eV at temperatures from 300 to 770 K in UHV using a rotating-analyzer ellipsometer.⁸ Similar ellipsometry measurements of Ni at room temperature were performed by Lenham and Treherne^{9,10} at selected infrared wavelengths between 5 and 20 μm. Lynch *et al.*¹¹ measured the absorptivity of single-crystalline Ni at 4.2 K from 0.08 to 3.0 eV using a calorimetric technique and determined the DF by the Kramers–Kronig transform. At higher photon energies (0.5–6.5 eV), Johnson and Christy¹² calculated the DF of evaporated semitransparent (20–50 nm thick) Ni thin films in the nitrogen atmosphere from transmission and reflection data. A review of the early DF results of Ni was given by Lynch and Hunter in Palik's handbook¹ and also by Adachi.³ More recently, ellipsometry measurements were also performed on Ni_{1–x}Pt_x thin films for applications in semiconductor manufacturing metrology.^{4,13,14}

Considering the advances in spectroscopic ellipsometry and vacuum techniques over the last 50 years, it seems worthwhile to revisit the optical constants of Ni and determine the DF

from 0.06 to 6.0 eV with improved accuracy. We tabulate parameters to calculate the optical constants of Ni using model DFs. We are particularly interested in the relative contributions to ϵ from free carriers and interband optical transitions. We also study the frequency dependence of the scattering rate and of the plasma frequency.

II. EXPERIMENTAL METHODS

Several 10 × 10 mm² substrates of cold-rolled polycrystalline Ni (>99.9% purity) with 1 mm thickness were obtained commercially.¹⁵ No preferred orientation was seen with powder x-ray diffraction. These pieces had a grain size of 10–50 μm and an rms surface roughness of 1–3 nm (measured with atomic force microscopy in 20 × 20 μm² scans and x-ray reflectance). Before our ellipsometry measurements, all samples were heated to 750 K for 6 h in UHV to remove adsorbed overlayers and then kept in vacuum during the measurements. No significant change in surface roughness was observed after annealing in UHV.

It was reported previously¹⁶ that there is an anomaly in the optical response of Ni (bulk single- or polycrystalline or sputtered thin film) as the sample is heated in UHV beyond the Curie temperature (627 K) (see Fig. 1). Initially, we attributed this anomaly to three potential causes: (i) changes in the magnetic structure (transition between ferromagnetic and paramagnetic phase at the Curie temperature), (ii) bulk crystal structure of the sample, for example, grain growth after annealing,¹⁷ and (iii) surface overlayers.

Since we find this anomaly in single-crystalline and polycrystalline bulk substrates as well as in thin layers [see Fig. S1 (Ref. 45)], we conclude that the grain size or other structural changes due to annealing are not a likely cause of our anomaly. Since it is irreversible (only occurs during the initial heating of the substrate) and cannot be restored by placing the sample in a saturating magnetic field, while the phase transition (ferromagnetic to paramagnetic) at the Curie temperature is reversible, the anomaly cannot be a magnetic effect. The most likely explanation for this anomaly

Note: This paper is part of the Conference Collection: 8th International Conference on Spectroscopic Ellipsometry 2019, ICSE.

^{a)}Email: zollner@nmsu.edu. URL: <http://ellipsometry.nmsu.edu>.



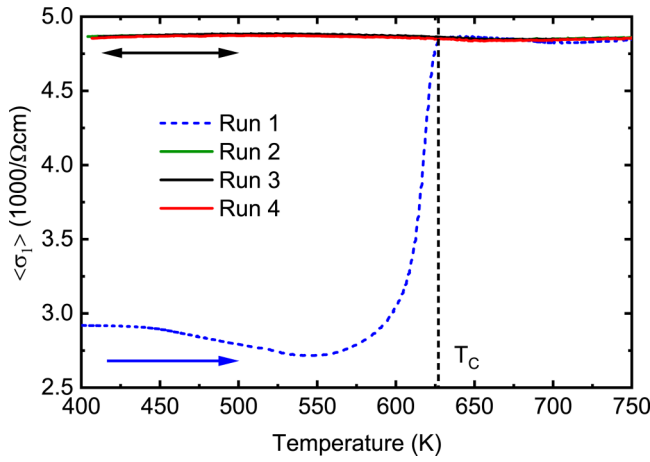


FIG. 1. Optical pseudoconductivity of a 1000 Å thick Ni layer on thick SiO₂ on an Si substrate as a function of temperature, measured by ellipsometry in ultrahigh vacuum at a single photon energy of 1.97 eV at an incidence angle of 70°. Compare Fig. S1 (Ref. 45) with data for polycrystalline and single-crystalline Ni.

is, therefore, degassing of the sample surface, for example, by evaporation of adsorbed overlayers. Additional details are given in the supplementary material.⁴⁵ Heating the Ni sample in UHV was the most effective cleaning method we were able to find.

The ellipsometric angles from 0.06 to 6.0 eV at 70° incidence angle were acquired at room temperature on two different ellipsometers (J. A. Woollam FTIR-VASE and J. A. Woollam VASE, Lincoln, NE) as described elsewhere.¹⁸ From 0.5 to 6.0 eV, we used a commercial UHV chamber (Janis Research ST-400, Woburn, MA) with strain-free quartz windows.¹⁶ From 0.06 to 0.9 eV, we used a similar chamber but with ZnSe windows. Changes in the polarization of the beam by the windows were corrected with a proprietary algorithm of the supplier. For data analysis, we assumed a surface roughness thickness of 20 Å. The surface roughness was described within the Bruggeman effective medium approximation as a 50/50 mixture of Ni and voids.¹⁹

A similar experimental setup for rotating-analyzer ellipsometry measurements using Drude's method from 0.46 to 5.9 eV at temperatures from 77 to 950 K in an UHV chamber was already described in 1967 by Pells.⁸ We extend this method further into the infrared spectral region with the use of a Fourier-transform spectrometer. Our setup also has increased accuracy due its computer-controlled Berek wave plate compensator and corrections for the effects of windows on the polarization of the incident and reflected light beam. Using their apparatus, Shiga and Pells⁷ showed that Ni could be cleaned by heating at 770 K for at least 12 h, confirming earlier photoemission results by Seib and Spicer.^{20,21}

III. EXPERIMENTAL RESULTS AND DATA ANALYSIS

The ellipsometric angles ψ and Δ for bulk cold-rolled polycrystalline Ni at room temperature are shown in Fig. 2 (symbols). If we assume a surface roughness of 20 Å, we can

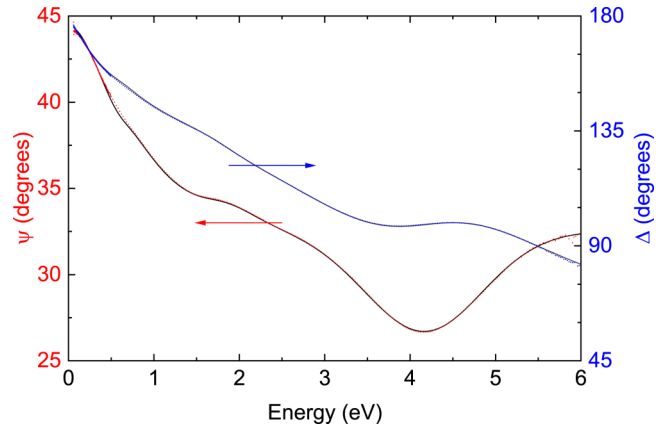


FIG. 2. Ellipsometric angles ψ and Δ of clean polycrystalline bulk Ni at room temperature (70 degrees angle of incidence). Symbols show experimental data and lines the best fit with a product model (5) with parameters in Table II.

directly calculate the DF $\epsilon(\omega)$ and the optical conductivity

$$\sigma(\omega) = -i\epsilon_0\omega[\epsilon(\omega) - 1] \quad (1)$$

from the ellipsometric angles¹⁹ (see Figs. 3 and 4). This is known as a point-by-point fit. We also fit these data using multi-band model DFs assuming 20 Å surface roughness (see below).

In our first multiband model, we write the DF as a sum of two Drude oscillators (to describe the optical response of free carriers) and several Lorentzians (to describe interband optical transitions of bound carriers)^{18,19}

$$\epsilon(\omega) = 1 + \chi_{\text{free}}(\omega) + \chi_{\text{bound}}(\omega), \quad (2)$$

$$\chi_{\text{free}}(\omega) = \sum_i \frac{\omega_{P,i}^2}{-\omega(\omega + i\gamma_{D,i})}, \quad (3)$$

$$\chi_{\text{bound}}(\omega) = \sum_i \frac{A_i\omega_{0,i}^2}{\omega_{0,i}^2 - \omega^2 - i\gamma_{0,i}\omega}, \quad (4)$$

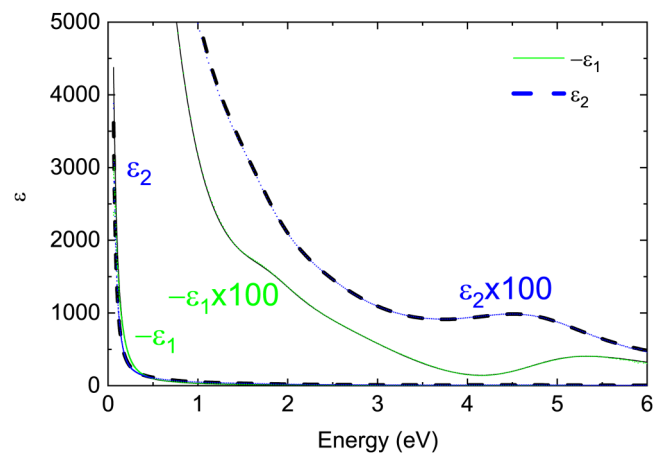


FIG. 3. Dielectric function of polycrystalline Ni determined from the ellipsometric angles shown in Fig. 2, assuming 2 nm surface roughness. Symbols show a point-by-point fit (without assuming a model dielectric function), while the lines show the dielectric function described by Eq. (5) with parameters in Table II.

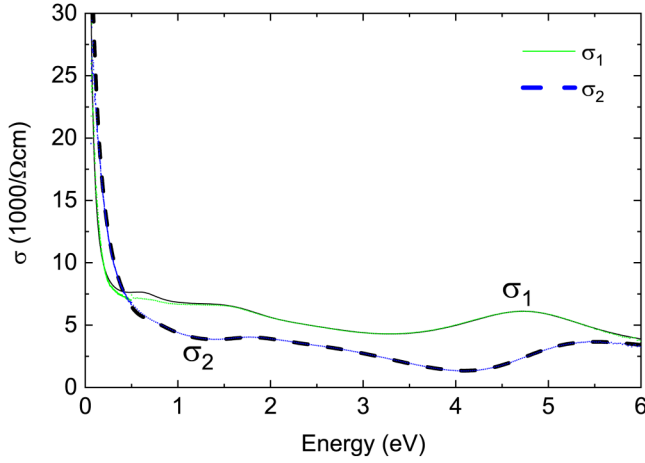


Fig. 4. Same data as in Fig. 3, but displayed as an optical conductivity.

where χ is the susceptibility, $\omega_{p,i} = n_i e^2 / \epsilon_0 m_i$ is the unscreened (unrenormalized, frequency-independent) plasma frequency, γ_D is the (unrenormalized, frequency-independent) Drude scattering rate, A is the dimensionless Lorentz amplitude, ω_0 is the resonance frequency, and γ_0 is the Lorentzian broadening. n_i is the density of the carrier species i , and m_i is its effective mass (also called the bare optical band mass).^{22–24} The parameters yielding the best fit to our data with this sum model are listed in Table I.

In our second multiband model, we write the dielectric function as a Kukharskii product^{18,25} of one Drude oscillator and several Lorentzians resulting in

$$\epsilon(\omega) = \frac{\omega_{LP}^2 - \omega^2 - i\gamma_{LP}\omega}{-\omega(\omega + i\gamma_D)} \prod_i \frac{\omega_{L,i}^2 - \omega^2 - i\gamma_{L,i}\omega}{\omega_{0,i}^2 - \omega^2 - i\gamma_{0,i}\omega}, \quad (5)$$

where ω_{LP} and γ_{LP} are the lower plasmon frequency and its broadening, while ω_0 is the Lorentz resonance frequency, and ω_L is the corresponding longitudinal frequency,¹⁸ where $\epsilon(\omega)$ crosses zero, with its broadening γ_L . (A second Drude factor was not needed to achieve a good fit.) The parameters

TABLE I. Parameters used to describe the optical constants of polycrystalline Ni with a sum model: amplitude A , plasma frequency ω_p , energy ω_0 , and broadening γ . All parameters are given with three significant digits. Due to parameter correlations, the uncertainty is probably much larger. The DC conductivity σ_0 was calculated from the Drude parameters using Eq. (S16) (Ref. 45).

	A	$\hbar\omega_p$	$\hbar\omega_0$	$\hbar\gamma$	σ_0
	(1)	(eV)	(eV)	(eV)	(1/ Ω cm)
Drude 1		11.9		2.87	6 640
Drude 2		4.86		0.0421	75 500
Lorentz 1	7.07		0.636	0.503	
Lorentz 2	3.52		1.56	1.06	
Lorentz 3	0.437		2.59	1.27	
Lorentz 4	2.90		4.80	2.17	
Lorentz 5	1.62		9.17	1.16	

resulting in the best fit to our data with this product model are given in Table II.

These two multiband models are identical only if the broadening parameters in the numerator and denominator are equal and much smaller than the differences between the resonance frequencies.¹⁸ The additional broadening parameters in the numerators of the second (Kukharskii product) model offer flexibility by adding different widths to the zeros and poles of the dielectric function. The lower plasmon frequency ω_{LP} is usually smaller than the plasma frequency ω_p due to the repulsion by the longitudinal frequencies ω_L of bound carriers, similar to plasmon-phonon coupling in the Raman or infrared spectra of doped semiconductors.^{18,25} See Ref. 18 for the motivation of both models, additional details, and historical references.

The best fit to the ellipsometric angles using the product model is shown by the lines in Fig. 2. The best fit with a sum model yields similar results. The difference between the model and the data is no more than 0.3° for ψ and no more than 0.7° for Δ . Typical experimental errors from the measurement are 0.01° for ψ and 0.1° for Δ . The average mean square deviation between data and model is lower than the experimental errors, but there is a statistically significant difference between the data and both multiband models from 0.5 to 1.0 eV, which we could not reduce with the addition of another oscillator.

The dielectric functions from the point-by-point fit and from the product model (5) are shown in Fig. 3. The corresponding optical conductivities are shown in Fig. 4. The loss function $-1/\epsilon$ is given in Fig. 5. We also show the complex refractive index in Fig. S3 (Ref. 45), and the absorption coefficient and the penetration depth in Fig. S4.⁴⁵ The complex impedance in the infrared spectral region is shown in Fig. S10.⁴⁵

The third model to describe the optical constants of a metal assumes that the optical conductivity is due to a single species of free carriers (single-band model), leading to an optical conductivity of the form

$$\sigma(\omega) = \frac{\epsilon_0 \omega_p^2}{\gamma - i\omega} = \frac{\epsilon_0 \omega_p^2 \tau}{1 - i\omega\tau} = \frac{ne^2 \tau}{m(1 - i\omega\tau)}. \quad (6)$$

TABLE II. Parameters (in units of electron volts) used to describe the optical constants of polycrystalline Ni with a product model: longitudinal and transverse frequencies ω_0 and ω_L (or ω_{LP}) and the related broadenings γ_0 (or γ_D) and γ_L (or γ_{LP} for the Drude factor). All parameters are given with three significant digits. Due to parameter correlations, the uncertainty is probably much larger. (f) indicates that the parameter was fixed.

	$\hbar\omega_0$	$\hbar\gamma_0$	$\hbar\omega_L$	$\hbar\gamma_L$
Drude	0	0.0426	0.693	0.519
Lorentz 1	0.696	0.468	1.21	3.15
Lorentz 2	1.88	0.916	1.92	0.956
Lorentz 3	2.82	3.67	3.80	2.08
Lorentz 4	4.85	2.23	7.38	2.21
Lorentz 5	9.73	1.0(f)	19.5	1.0(f)

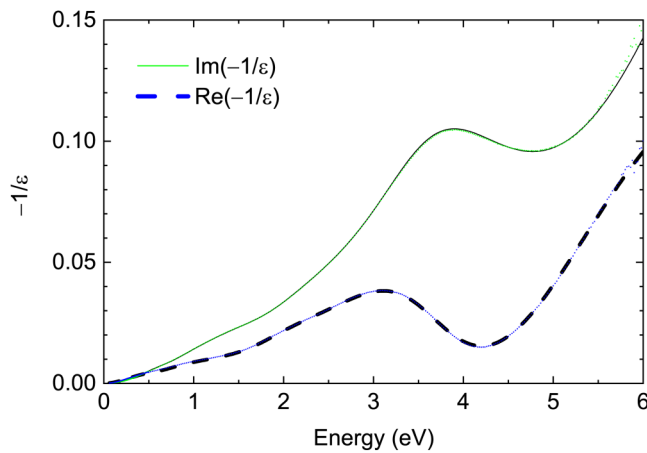


FIG. 5. Same data as in Fig. 3, but as a loss function $-1/\epsilon$.

If the Drude model with a single free-carrier species truly describes the optical constants, then γ , τ , and m are frequency-independent constants. If, however, there is more than one carrier species or if the carriers interact with other elementary excitations or if there is a contribution to the conductivity from infrared-active optical phonons or interband transitions, then the scattering rate and mass need to be renormalized and depend on the angular frequency ω . The supplementary material (Ref. 45) lists the equations and how these frequency-dependent quantities can be calculated.²⁴ This method has been used to describe the optical constants of alkali metals,²³ heavy Fermion compounds,^{24,26} or correlated conducting metal oxides.^{27–30} While this method has often been applied to investigate and interpret the optical conductivity determined from reflectance measurements, it is not widely known in the ellipsometry community. We are not aware of an application of this technique to transition metals with two species of free carriers.

IV. DISCUSSION

A. Optical constants

There are significant differences between our optical constants and those in the literature^{1,4,12} (see Fig. 6). Our *in situ* data of a polycrystalline Ni sample cleaned by heating and corrected for 2 nm surface roughness show the highest (lowest) values of ϵ_2 (ϵ_1) and, therefore, likely represent the most pristine surface compared to other experiments (see Fig. S2).⁴⁵ It is not likely that we overcorrected our ellipsometric angles to obtain the dielectric function, since our surface roughness was determined by atomic force microscopy and x-ray reflectance.

Johnson and Christy¹² as well as Vehse and Arakawa³¹ briefly exposed their layers to air and measured in N_2 gas, likely leading to an adsorbed water layer, similar to Abdallah *et al.*⁴ In the near-infrared region, our ϵ_1 data agree well with those of Johnson and Christy,¹² but there is a large discrepancy for ϵ_2 . This might also be related to cleaning (see Fig. S2).⁴⁵ Data from Ref. 1 below 3.0 eV were acquired at 4 K on single crystals. Therefore, the structure at 1.5 eV is

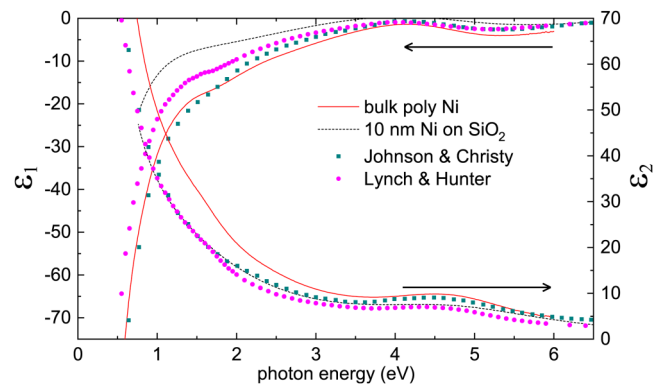


FIG. 6. Comparison of the dielectric function of Ni from this work on bulk polycrystalline Ni (solid), a 10 nm thick Ni layer (Ref. 4) on SiO_2 (dotted), from transmission and reflectance measurements of thin layers by Johnson and Christy (Ref. 12) at 300 K and as tabulated by Lynch and Hunter (Ref. 1) (at 300 K above 3.1 eV and at 4 K below 3.0 eV).

much more pronounced than in our data taken at 300 K. Also, the Drude scattering rate is expected to be much smaller at low temperatures, and, therefore, the Drude divergence should be sharper at 4 K. This might explain the difference between our data and those listed by Lynch and Hunter¹ in the near-infrared. Above 3.1 eV, Ref. 1 reports data from Vehse and Arakawa³¹ on a sample exposed to air that might not have been as clean as ours. In the infrared, differences between our impedance (Fig. S10)⁴⁵ and that of Lenham and Treherne¹⁰ are likely related to the lower scattering rate of single crystals compared to polycrystalline Ni. Losurdo *et al.*¹⁷ report $\langle \epsilon_1 \rangle = -1.0$ and $\langle \kappa \rangle = 2.1$ at 4.2 eV. This compares well with our roughness-corrected results of $\epsilon = -1.4 + 9.6i$ (or $\kappa = 2.4$).

B. Interband transitions

The spin-polarized band structure of Ni, including Fermi surfaces, effective masses, and optical conductivity, has been discussed by Ehrenreich *et al.*³² and by Wang and Callaway,^{33–35} as well as others.^{4,36,37} Electronic states near the Fermi level are comprised of sp- and d-orbitals. Because of ferromagnetic ordering, there is a considerable exchange splitting³⁸ (about 0.5 eV) between the majority (spin-up) and minority spin (spin-down) d-orbitals. The spin-up band is completely full, while the spin-down d-orbital crosses the Fermi surface. Therefore, we expect d-intraband transitions at arbitrarily low energies, as well as interband transitions between sp- and d-orbitals.

References 33 and 35 predict interband transitions at 0.3 eV (buried in the Drude background in our room-temperature data, but perhaps observable in low-temperature ellipsometry measurements), 0.8 eV (between parallel d-bands related to the exchange splitting), 2 or 2.5 eV, and between 5.1 and 5.5 eV (from the lower d-bands to the sp-bands above the Fermi energy). The latter peak can be lowered to 4.8 eV by self-energy corrections. Several regions in the Brillouin zone contribute to these transitions. Due to spin-orbit splitting, spin-flip interband transitions are weakly allowed.³⁵

An inspection of the ellipsometric angle ψ at low photon energies shows immediately that Ni is not a good Drude metal. ψ is related to the reflectivity R and $\psi = 45^\circ$ is

equivalent to $R = 1$. In a Drude metal [compare gold in Fig. S11 (Ref. 45)], ψ remains near 45° until the onset of interband transitions (near 2.5 eV for Au). In Ni, ψ drops nearly linearly from 44.3° at 0.06 eV to 35.1° at 1.3 eV (for an incidence angle of 70°). Therefore, intraband transitions occur at very low energies, as expected from the partially filled d-band.

It is difficult to quantify the interband transitions in our dielectric function (Fig. 3) because the Drude contribution is dominant at low energies. Therefore, we subtract the Drude contribution (3) from our multiband sum model (2) and plot the remaining interband contribution (4) in Fig. S5.⁴⁵ The parameter correlations for our Drude–Lorentz model are below 0.9 (not as bad as it could be). Nevertheless, this subtraction method is somewhat arbitrary because it depends on the number of oscillators and whether they are characterized as Drude or Lorentz oscillators. This was already pointed out by Ehrenreich *et al.*³² Our best model in Table I has strong Lorentz peaks in ϵ_2 at 0.6, 1.5, and 4.7 eV and a shoulder at 2.5 eV. This is, of course, related to the Lorentzian resonance energies listed in Table I. The sum of the Lorentzian amplitudes yields $\epsilon_\infty = \sum A_i = 15.5$. A significant contribution to ϵ_∞ is from the lowest peak at 0.64 eV. The broadenings of the interband transitions are quite large, between 0.5 and 2.2 eV. The temperature dependence of interband transition energies and broadenings will be published elsewhere. In general, the agreement between our Drude–Lorentz model (2) and theory^{33,35} is excellent.

Our product model (5) also shows five interband transitions with energies and broadenings similar to the Drude–Lorentz model (2), but separating the Drude and interband contributions in the product model is not straightforward.

Lynch *et al.*¹¹ report several infrared peaks below 1 eV in their absorption (calorimetry) measurements at 4 K. These peaks are absent in our analysis, see Table I, possibly because the free-carrier absorption in our results at 300 K overwhelms these interband transitions. Our results agree on interband transition peaks near 1.5 eV. Our peak at 2.6 eV was also found in ellipsometry measurements at 77 K by Stoll,^{39,40} but we do not observe any fine structure due to spin–orbit splitting.

Johnson and Christy,¹² Shiga and Pells,⁷ as well as Abdallah *et al.*⁴ report a strong conductivity or ϵ_2 peak at 4.8 eV, which is also present in our data. As mentioned, it arises from transitions from the lower d-orbital to the sp-like bands. Shiga and Pells⁷ report that the peak at 4.8 eV is a superposition of two peaks separated by an energy difference, which is proportional to spontaneous magnetization. This energy difference may be related to the exchange splitting. They show that the broadening of this peak has an anomalous temperature dependence, which decreases with increasing temperature. The width of our 4.8 eV peak is indeed quite large (2.1 eV), but we could not improve our fit with two separate contributions. We will revisit this topic when we report temperature-dependent ellipsometry results for Ni.

C. Free-carrier properties

The only Drude parameters reported previously for Ni that we are aware of are those of Lenham and Treherne⁴¹ cited by

Wang and Callaway:³³ $n = 6.5 \times 10^{21} \text{ cm}^{-3}$, $E_p = 2.99 \text{ eV}$ (assuming an optical mass m_0 , the electron mass in vacuum), $\sigma_0 = 186\,000/\Omega \text{ cm}$ ($18.6 \times 10^{15}/\text{s}$ in Gaussian units), and $\tau = 11.3 \text{ fs}$ ($\Gamma = 58 \text{ meV}$). Lynch *et al.*¹¹ report a Drude scattering rate of $\Gamma = 20 \text{ eV}$ at 4 K, which is unphysically large because of the anomalous skin effect.¹ However, their value of $\sigma_0 = 658\,000/\Omega \text{ cm}$ is quite reasonable at 4 K.

In the limit of high frequencies (but below the onset of interband transitions) and low scattering ($\omega\tau \gg 1$), the dielectric function of a Drude metal is approximated by

$$\epsilon_1(\omega) \approx \epsilon_\infty - \frac{\omega_p^2}{\omega^2} = \epsilon_\infty - \frac{E_p^2}{E^2}, \quad (7)$$

where ϵ_∞ is the high-frequency dielectric constant, i.e., the contribution to ϵ by bound charges. It is, therefore, customary^{41–43} to plot ϵ_1 vs $1/E^2$, which yields ϵ_∞ as the intercept and E_p^2 as the slope. This technique was used by Lenham and Treherne⁴¹ to find $E_p = 2.99 \text{ eV}$, from which they calculated the carrier density $n = 6.5 \times 10^{21} \text{ cm}^{-3}$ (assuming an optical mass of m_0). Our data and a linear interpolation are shown in Fig. 7(a). Our linear regression to the data for $1/E^2 < 30$ (0.18–6.0 eV) finds a plasma frequency of 4.7 eV, which is consistent with one of the plasma frequencies found in our sum model (see Table I). We also find an unphysical (negative) value of $\epsilon_\infty = -5.4$. We expect $\epsilon_\infty \approx 15$ (see Fig. S5).⁴⁵ A linear fit over the entire spectral range from 0.06 to 6.0 eV finds a plasma frequency of 3.7 eV, which is similar to the energy of the main loss function peak (see Fig. 5). If we fit from 71 to 100 meV (our lowest-frequency data), we find $E_p = 3.4 \text{ eV}$. We see that this interpolation scheme only yields a rough estimate of the plasma frequency for one of the two carrier species.

To calculate the carrier density, we need to know the optical (effective) masses. Ehrenreich *et al.*³² find an optical mass of 1.4 for s-electrons and 3.5 for d-electrons. If we associate the Drude term with small $\Gamma = 42 \text{ meV}$ (Drude 2) with s-electrons, then $E_p = 4.86 \text{ eV}$ results in an electron density of $24 \times 10^{21} \text{ cm}^{-3}$ (0.26 e/atom). Similarly, if the Drude 1 term with $\Gamma = 2.87 \text{ eV}$ and $E_p = 11.9 \text{ eV}$ arises from d-electrons, then the carrier density is $359 \times 10^{21} \text{ cm}^{-3}$ (3.9 e/atom). We thus find a total density of about 4.2 e/atom from our optical measurements (assuming masses from Ref. 32), less than half of the expected density of 10 electrons per atom. Similarly, if we use effective masses calculated by Wang and Callaway,³³ we overestimate e/atom.

In the same high-frequency limit ($\omega\tau \gg 1$), we also find

$$\epsilon_2(\omega) \approx \frac{\omega_p^2}{\omega^2} \times \frac{1}{\omega\tau} = \frac{E_p^2 \Gamma}{E^2 E}. \quad (8)$$

One, therefore, plots⁴³ $\epsilon_2 E$ vs $1/E^2$, which should yield (for a Drude metal) a straight line through the origin with a slope of $E_p^2 \Gamma$. If E_p is found from the plot of ϵ_1 vs $1/E^2$ (as discussed above), then one can calculate the scattering rate Γ . We apply this analysis method to our data in Fig. 7(b) and find a slope of $E_p^2 \Gamma = 0.82 \text{ eV}^3$, which agrees well with the results listed in Table I, where we find $E_p^2 \Gamma = 0.77 \text{ eV}^3$ for

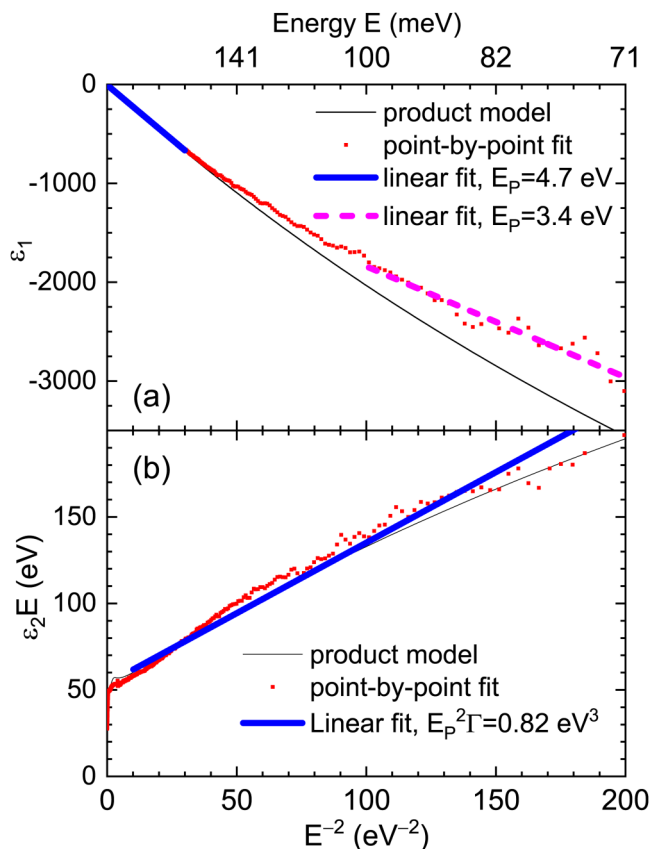


FIG. 7. Drude parameters of polycrystalline Ni at 300 K extracted from the dielectric function in the high-frequency, low-scattering limit ($\omega\tau \gg 1$) using (a) Eq. (7) and (b) Eq. (8).

one species of carriers. The positive (nonzero) intercept of the $\epsilon_2 E$ vs $1/E^2$ graph can be explained with the contributions of bound carriers to ϵ_2 (interband transitions).

Without having to rely on the $\omega\tau \gg 1$ limit, the Drude model implies²³

$$\epsilon_1(\omega) = 1 - \omega\tau\epsilon_2(\omega) = 1 - \frac{1}{\Gamma}\epsilon_2(E)E. \quad (9)$$

One, therefore, plots ϵ_1 vs $\epsilon_2 E$, which should yield $-1/\Gamma$ as the slope. Using this method, Lenham and Treherne⁴¹ found $\Gamma = 58$ meV, which compares well with our Drude 2 broadening in Table I. As shown in Fig. 8, this graphical approach results in $\Gamma = 53$ meV for our data. This value is larger than $\Gamma = 42$ meV in Table I because of the discrepancy between the ellipsometry data and our Drude–Lorentz model in this energy range (compare the line and symbols in Fig. 8).

It has been argued that free-electron contributions to the optical constants of Ni are negligible^{12,43,44} because intra-band transitions between different partially filled d-orbitals are possible at arbitrarily low energies.¹ Nevertheless, our Drude–Lorentz model with two carrier species gives a remarkably good agreement with our near-infrared and visible optical constants of Ni. Since we use two free carrier species with different plasma frequencies and broadenings, there is a significant Drude contribution even at 6 eV (see Fig. S5).⁴⁵ The usual graphical techniques,⁴³ when applied

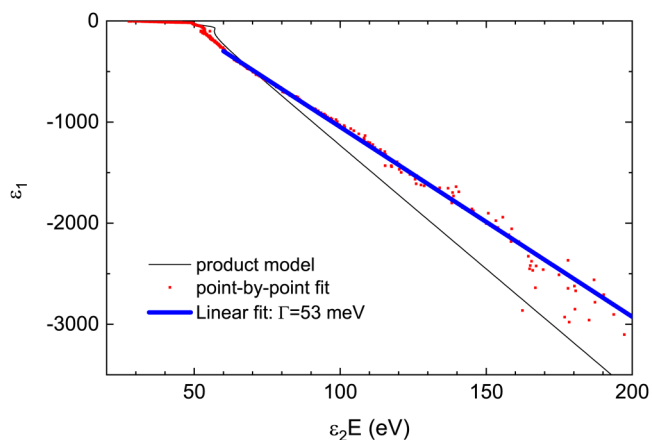


FIG. 8. Drude parameters of polycrystalline Ni at 300 K extracted from the dielectric function using Eq. (9).

to our infrared data, yield reasonable values for the plasma frequency and broadening without any modeling but only for species of carriers with the smaller broadening. The other Drude contribution (with large broadening) has a strong overlap with visible and UV interband transitions and, therefore, can only be extracted by fitting the ellipsometric angles with a Drude–Lorentz lineshape.

D. Frequency-dependent scattering rate

Instead of modeling our experimental data with multiband sum or product lineshapes, we can also attribute the entire optical response to a single Drude term with frequency-dependent scattering rate, effective mass, and plasma frequency,²⁴ as described in the supplementary material.⁴⁵ Between 0 and 2 eV, we see a nearly threefold increase of the plasma frequency in Fig. S7.⁴⁵ This can be explained as follows: at low energies, the Drude 2 term ($E_p = 4.86$ eV and $\Gamma = 42$ meV) dominates. At higher frequencies, the Drude 1 term with its larger broadening ($E_p = 11.9$ eV, $\Gamma = 2.87$ eV) becomes more important, roughly explaining the threefold increase in E_p . Above 2 eV, the frequency-dependent plasma frequency is dominated by interband transitions, leading to a large peak at 4.3 eV.

Similarly, the frequency-dependent renormalized scattering rate shown in Fig. S8⁴⁵ is small (about 50 meV) at low energies, dominated by the Drude 2 term. It increases nearly linearly (with a quadratic onset at very low energies) and flattens out above 1 eV at a value of 2.4 eV, similar to the scattering rate of the Drude 1 term.

V. SUMMARY

We used thermal cleaning in UHV to prepare a nearly pristine polycrystalline Ni surface. With in situ spectroscopic ellipsometry from 0.06 to 6.0 eV on two different instruments, we determined the ellipsometric angles and the optical constants of Ni, superseding the 50 year-old literature data from various sources. Our data can be described well with a multiband Drude–Lorentz model. Parameters are listed and can be used to calculate reference dielectric functions for Ni. Our

model separates contributions to the optical constants from free carriers and interband transitions. We require two species of carriers (perhaps sp- and d-electrons) to describe our data, with very different plasma frequencies and scattering rates. Despite earlier claims to the contrary, graphical methods to extract free-carrier properties from the optical constants work quite well. We also find broad d-intraband transitions even at our lowest energies. At higher photon energies, several interband transitions take place, which agrees well with previous studies.

ACKNOWLEDGMENTS

This work was supported by the National Science Foundation (NSF, No. DMR-1505172), the European Union Structural and Investment Funds, and the Czech Ministry of Education, Youth, and Sports (No. CZ.02.2.69/0.0/0.0/16_027/0008215, Project IOP Researchers Mobility).

- ¹D. W. Lynch and W. R. Hunter, *Handbook of Optical Constants*, edited by E. D. Palik (Academic, San Diego, 1985), Vol. I, p. 313.
- ²M. A. Ordal, L. L. Long, R. J. Bell, S. E. Bell, R. R. Bell, R. W. Alexander, and C. A. Ward, *Appl. Opt.* **22**, 1099 (1983).
- ³S. Adachi, *The Handbook on Optical Constants of Metals* (World Scientific, Singapore, 2012), p. 334.
- ⁴L. Abdallah, T. M. Tawalbeh, I. V. Vasiliev, S. Zollner, C. Lavoie, A. Ozcan, and M. Raymond, *AIP Adv.* **4**, 017101 (2014).
- ⁵G. E. Jellison, *Appl. Opt.* **38**, 4784 (1999).
- ⁶L. Jin, S. Kasuga, and E. Kondoh, *Opt. Express* **22**, 27811 (2014).
- ⁷M. Shiga and G. P. Pells, *J. Phys. C* **2**, 1847 (1969).
- ⁸G. P. Pells, *J. Sci. Instrum.* **44**, 997 (1967).
- ⁹A. P. Lenham and D. M. Treherne, *J. Opt. Soc. Am.* **56**, 1076 (1966).
- ¹⁰A. P. Lenham and D. M. Treherne, *J. Opt. Soc. Am.* **57**, 476 (1967).
- ¹¹D. W. Lynch, R. Rosei, and J. H. Weaver, *Solid State Commun.* **9**, 2195 (1971).
- ¹²P. B. Johnson and R. W. Christy, *Phys. Rev. B* **9**, 5056 (1974).
- ¹³V. K. Kamineni, M. Raymond, E. J. Bersch, B. B. Doris, and A. C. Diebold, *J. Appl. Phys.* **107**, 093525 (2010).
- ¹⁴L. S. Abdallah, Ph.D. thesis (New Mexico State University, Las Cruces, NM 2014).
- ¹⁵MTI Corporation, 860 S. 19th Street, Richmond, CA 94804.
- ¹⁶S. Zollner, T. N. Nunley, D. P. Trujillo, L. G. Pineda, and L. S. Abdallah, *Appl. Surf. Sci.* **421**, 913 (2017).
- ¹⁷M. Losurdo, M. M. Giangregorio, O. Capezzuto, and G. Bruno, *J. Phys. Chem. C* **115**, 21804 (2011).
- ¹⁸S. Zollner, P. P. Paradis, F. Abadizaman, and N. S. Samarasingha, *J. Vac. Sci. Technol. B* **37**, 012904 (2019).
- ¹⁹H. Fujiwara, *Spectroscopic Ellipsometry* (Wiley, West Sussex, 2007).
- ²⁰D. H. Seib and W. E. Spicer, *Phys. Rev. Lett.* **20**, 1441 (1968).
- ²¹D. H. Seib and W. E. Spicer, *Phys. Rev. B* **2**, 1694 (1970).
- ²²J. W. Allen and J. C. Mikkelsen, *Phys. Rev. B* **15**, 2952 (1977).
- ²³A. J. Sievers, *Phys. Rev. B* **22**, 1600 (1980).
- ²⁴P. E. Sulewski, A. J. Sievers, M. B. Maple, M. S. Torikachvili, J. L. Smith, and Z. Fisk, *Phys. Rev. B* **38**, 5338 (1988).
- ²⁵M. Schubert, *Infrared Ellipsometry on Semiconductor Layer Structures: Phonons, Plasmons, and Polaritons* (Springer, Berlin, 2004).
- ²⁶B. C. Webb, A. J. Sievers, and T. Mihalisin, *Phys. Rev. Lett.* **57**, 1951 (1986).
- ²⁷G. A. Thomas, J. Orenstein, D. H. Rapkine, M. Capizzi, A. J. Millis, R. N. Bhatt, L. F. Schneemeyer, and J. V. Waszczak, *Phys. Rev. Lett.* **61**, 1313 (1988).
- ²⁸R. T. Collins, Z. Schlesinger, F. Holtzberg, P. Chaudhari, and C. Feild, *Phys. Rev. B* **39**, 6571 (1989).
- ²⁹Z. Schlesinger, R. T. Collins, F. Holtzberg, C. Feild, S. H. Blanton, U. Welp, G. W. Crabtree, Y. Fang, and J. Z. Liu, *Phys. Rev. Lett.* **65**, 801 (1990).
- ³⁰P. Kostic, Y. Okada, N. C. Collins, Z. Schlesinger, J. W. Reiner, L. Klein, A. Kapitulnik, T. H. Geballe, and M. R. Beasley, *Phys. Rev. Lett.* **81**, 2498 (1998).
- ³¹R. C. Vehse and E. T. Arakawa, *Phys. Rev.* **180**, 695 (1969).
- ³²H. Ehrenreich, H. R. Philipp, and D. J. Olechna, *Phys. Rev.* **131**, 2469 (1963).
- ³³C. S. Wang and J. Callaway, *Phys. Rev. B* **9**, 4897 (1974).
- ³⁴C. S. Wang and J. Callaway, *Phys. Rev. B* **15**, 298 (1977).
- ³⁵D. G. Laurent, J. Callaway, and C. S. Wang, *Phys. Rev. B* **20**, 1134 (1979).
- ³⁶W. Hübner, *Phys. Rev. B* **42**, 11553 (1990).
- ³⁷K. Doll, *Surf. Sci.* **544**, 103 (2003).
- ³⁸E. Dietz, U. Gerhardt, and C. J. Maetz, *Phys. Rev. Lett.* **40**, 892 (1978).
- ³⁹M.-P. Stoll, *Solid State Commun.* **8**, 1207 (1970).
- ⁴⁰M.-P. Stoll, *J. Appl. Phys.* **42**, 1717 (1971).
- ⁴¹A. P. Lenham and D. M. Treherne, *Optical Properties and Electronic Structure of Metals and Alloys*, edited by F. Abelés (North Holland, Amsterdam, 1966), pp. 196–201.
- ⁴²R. E. Lindquist and A. W. Ewald, *Phys. Rev.* **135**, A191 (1964).
- ⁴³P. B. Johnson and R. W. Christy, *Phys. Rev. B* **11**, 1315 (1975).
- ⁴⁴I. I. Sasovskaya and M. M. Noskov, *Fiz. Met. Metallov.* **32**, 723 (1971).
- ⁴⁵See supplementary material at <https://doi.org/10.1116/1.5118841> for additional experimental data (especially ellipsometry results before and after annealing) and different representations of the optical constants, a detailed description of the Drude model (including equations to calculate the frequency-dependent renormalized scattering rate and plasma frequency), the definition of the complex optical impedance, an overview of the anomalous skin effect and why it was ignored for this work, a discussion of the Kukharskii model for metals with two species of free carriers, and preliminary results on the optical constants of gold (in comparison to Ni) from ellipsometry measurements.

Supplementary Material:

Optical constants of polycrystalline Ni from 0.06 to 6.0 eV at 300 K

(Dated: 26 October 2019)

Farzin Abadizaman¹ and Stefan Zollner^{1,2}

¹*Department of Physics, New Mexico State University, P.O. Box 30001, Las Cruces, NM 88003, USA*

²*Fyzikální ústav AV ČR, v.v.i., Sekce optiky, Na Slovance 2, CZ-18221 Praha 8, Czech Republic*

S1. OPTICAL CONSTANTS ANOMALY OF NI NEAR THE CURIE TEMPERATURE

The optical pseudo-conductivity $\langle\sigma_1\rangle$ at 1.97 eV for three different Ni samples as a function of temperature is shown in Fig. S1, determined using spectroscopic ellipsometry at a 70° incidence angle. All data were acquired in UHV with a pressure below 10^{-8} Torr, to avoid surface contamination. During the first run (blue), the temperature of the sample was increased slowly from room temperature to 750 K. The heater was then turned down slowly and we measured $\langle\sigma_1\rangle$ as the sample cooled down to 400 K (run 2, green). We then turned the heater on again and heated the sample again to 750 K (run 3, black). Finally (run 4, red), we turned the heater down again and measured $\langle\sigma_1\rangle$ as the sample cooled down. Similar data for the pseudo-dielectric function of polycrystalline Ni were reported previously.¹⁶

All Ni samples show an anomaly in the optical pseudo-conductivity at elevated temperatures, where there is a rapid rise of $\langle\sigma_1\rangle$. Since the temperature was measured with a thermocouple attached to the sample, it is difficult to obtain accurate temperature readings. Errors of up to 50 K are possible. Therefore, the temperature where the rise of $\langle\sigma_1\rangle$ occurs may or may not be the same for all samples, due to these errors.

The anomaly occurs only during the first heating of the sample past the Curie temperature. Since magnetic phase transitions (ferromagnetic to paramagnetic) should be reversible, it is not likely that the anomaly is due to magnetic effects. The anomaly could not be restored by removing the sample from the cryostat and placing into a saturating magnetic field of about 1 T. A partial restoration of the anomaly was possible by leaving the sample in humid air for several weeks. We therefore conclude that the anomaly is not due to magnetic effects as argued previously,¹⁶ but due to changes in surface conditions. We attribute the initial low-temperature pseudo-conductivity for each sample to different adsorbed surface layers (which were removed by the initial heating of the Ni sample). It was reported previously⁴ that about 50 Å of water can be removed from the surface of thin Ni layers by heating in UHV. After heating, when adsorbed overlayers have evaporated, the final optical pseudo-conductivity is due to different surface roughness

conditions (or other overlayers that cannot be removed by heating) or due to different bulk conduction mechanisms. For example, single-crystalline Ni is expected to be more conducting than cold-rolled poly-crystalline Ni.

We conclude that heating our Ni samples above the Curie temperature for about six hours is an effective way of preparing Ni surfaces for optical constants measurements. This cleaning procedure was therefore used for all ellipsometry measurements on Ni described in this work. To demonstrate the impact of cleaning, we show the room-temperature ellipsometric angles and the pseudo-dielectric function of cold-rolled pseudo-crystalline Ni in Fig. S2. The ellipsometric angle ψ decreases and Δ increases, as adsorbed layers are removed by heating, especially near the critical point at 4.8 eV. Changes in the ellipsometric angles are smaller in the near-infrared below 1 eV than in the UV. Similarly, $\langle\epsilon_1\rangle$ decreases and

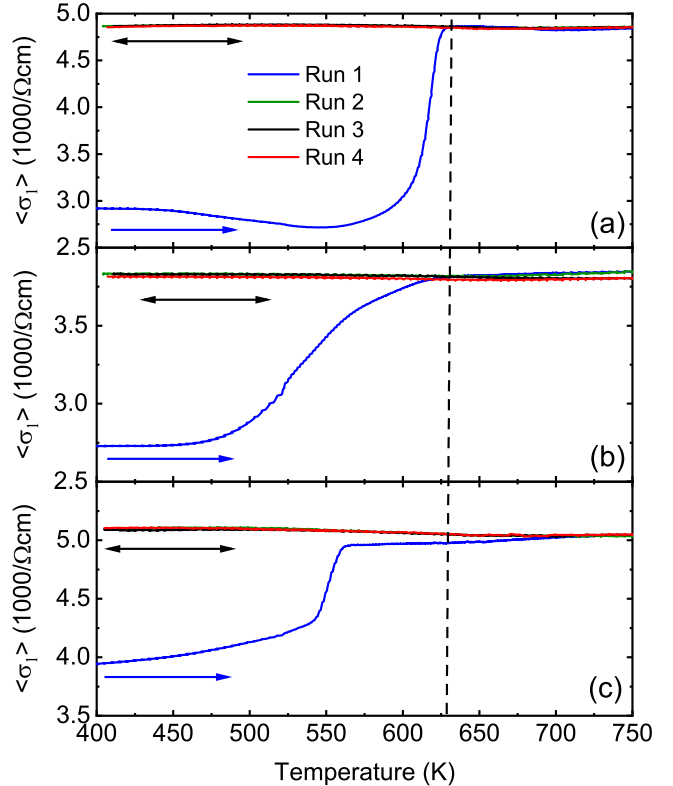


FIG. S1. Optical pseudo-conductivity $\langle\sigma_1\rangle$ as a function of temperature, measured by ellipsometry in ultra-high vacuum at a single photon energy of 1.97 eV at an incidence angle of 70° for (a) a 1000 Å thick sputtered Ni layer on thick SiO₂ on Si, (b) a bulk polycrystalline cold-rolled Ni substrate, (c) a single-crystalline Ni (001) substrate. The dashed vertical line shows the Curie temperature.

$\langle \epsilon_2 \rangle$ increases after heating of the sample. The largest changes of $\langle \epsilon \rangle$ are observed in the near-infrared spectral region.

In vacuum technology processing (for example in the semiconductor industry), heating of a wafer in vacuum is known as degassing. The experiments described in this section essentially monitor the degassing of Ni by *in situ* spectroscopic ellipsometry.

Similar changes in the ellipsometric angles and the pseudo-DF after heating in H_2 or exposure to O_2 have been reported by others¹⁷ (Hanekamp 1983). Slow annealing of an amorphous as-sputtered Ni layer in H_2 promotes crystallization and desorption of surface layers.¹⁷ This leads to a *decrease* of $\langle \epsilon_1 \rangle$ by 1.4 and an increase in $\langle \kappa \rangle$ by 1.0 at 4.2 eV. (If the sample remains in H_2 too long at high temperatures, nickel hydrides may form, which deteriorates the pseudo-DF again.) In our annealing experiments, we find an *increase* of our polycrystalline bulk Ni samples of $\langle \epsilon_1 \rangle$ by 0.2 and an increase in $\langle \kappa \rangle$ by 0.2 at 4.2 eV. This discrepancy of sign and magnitude can perhaps be explained by the fact that crystallization of an amorphous sputtered layer (associated with changes in position and broadening of the peak at 4.8 eV) and surface cleaning both contribute to the pseudo-DF. An energy of 4.2 eV may not be the best position for mon-

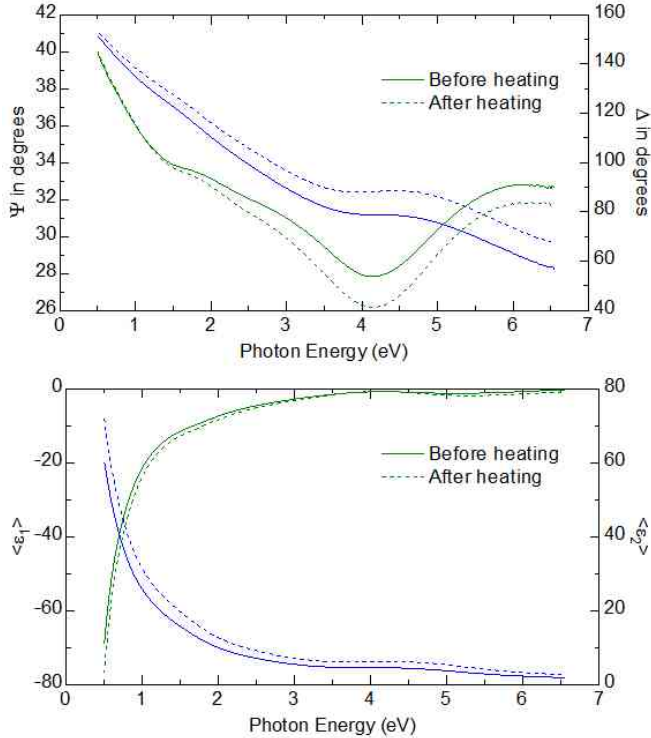


FIG. S2. Ellipsometric angles ψ and Δ at 70° incidence angle (top) and pseudodielectric function (bottom) as a function of photon energy for a cold-rolled polycrystalline Ni substrate at room temperature, acquired in a UHV cryostat before (solid) and after (dashed) heating to 750 K for 6 hours. ψ and $\langle \epsilon_1 \rangle$ are shown in green, Δ and in $\langle \epsilon_2 \rangle$ blue.

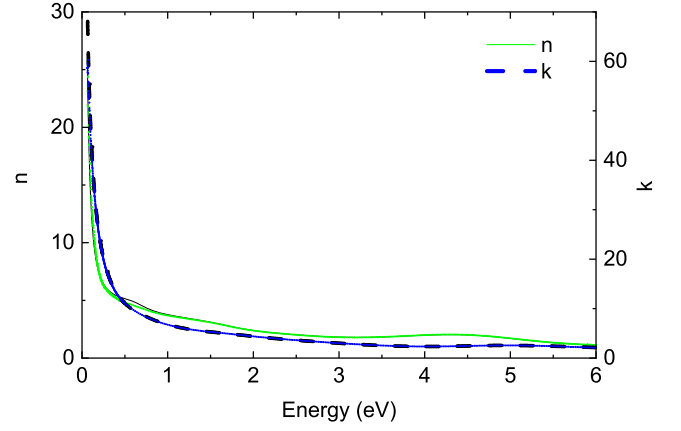


FIG. S3. Complex refractive index of polycrystalline Ni at 300 K calculated from the data shown in Fig. 3. Symbols show results from a point-by-point fit, lines the results from the product model using Eq. (5).

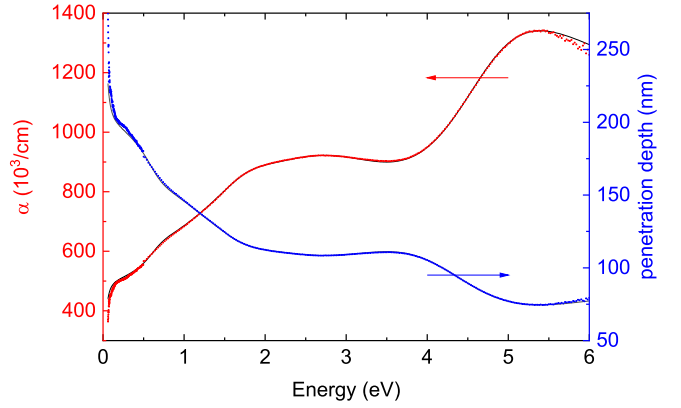


FIG. S4. Absorption coefficient and penetration depth of polycrystalline Ni at 300 K calculated from the data shown in Fig. 3. Symbols show results from a point-by-point fit, lines the results from the product model using Eq. (5).

itoring the cleanliness of a Ni surface. Hanekamp and van Silfhout (1983) show a decrease of Δ by about 1° at 1.97 eV after exposure to O_2 , significantly smaller than our observed change of 5° due to annealing.

S2. ADDITIONAL EXPERIMENTAL DATA

The complex refractive index calculated from the dielectric function of polycrystalline Ni is shown in Fig. S3. The absorption coefficient and penetration depth are shown in Fig. S4, the infrared complex impedance in Fig. S10. Separate Drude and Lorentz contributions to the total dielectric function in the sum model (2) are shown in Fig. S5. A spreadsheet with experimental and sum model data (ψ , Δ , ϵ_1 , ϵ_2 , n , k) versus photon energy is also available as supplementary material.

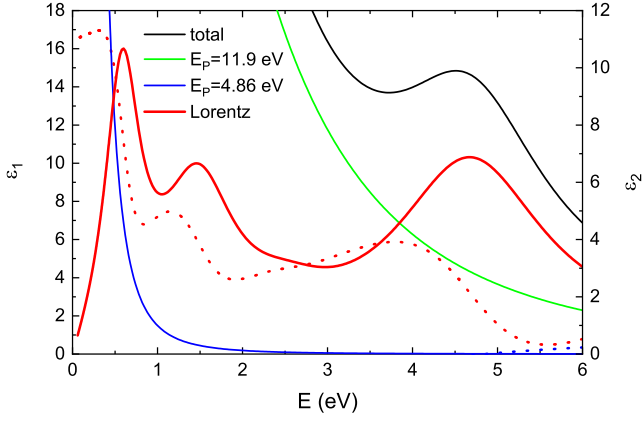


FIG. S5. Real (dotted) and imaginary (solid) parts of the dielectric function of Ni at 300 K calculated from the sum model (2), but showing the total contribution (black) as well as the Drude (green, blue) and Lorentz (red) contributions separately.

S3. DRUDE MODEL WITH FREQUENCY-DEPENDENT SCATTERING RATE

A. Drude dielectric function

Within the Drude model (for a single species of free carriers), the dielectric function ϵ versus angular frequency ω is written as¹⁹

$$\epsilon(\omega) = 1 - \frac{\omega_P^2}{\omega^2 + i\gamma\omega} = 1 + i \frac{\omega_P^2}{\omega(\gamma - i\omega)}, \quad (\text{S1})$$

where

$$\omega_P^2 = \frac{ne^2}{\epsilon_0 m} \quad (\text{S2})$$

is the *unscreened* plasma frequency and γ the scattering rate, with the carrier density n , the effective mass m (sometimes called *bare optical band mass*),²³ electronic charge e , and the permittivity of vacuum ϵ_0 . These equations assume that time-dependent fields vary like $e^{-i\omega t}$. Otherwise, all expressions in this section need to be replaced with their complex conjugates.

Some authors²³ add a high-frequency dielectric constant ϵ_∞ to the Drude expression (S1) and introduce an associated screened plasma frequency.¹⁸ We do not need this approach, because our models include explicit oscillators outside of our spectral range to consider the optical contribution from high-energy oscillators.

Written in real and imaginary components, Eq. (S1) becomes

$$\epsilon(\omega) = \epsilon_1(\omega) + i\epsilon_2(\omega) = 1 - \frac{\omega_P^2}{\omega^2 + \gamma^2} + i \frac{\omega_P^2}{\omega^2 + \gamma^2} \times \frac{\gamma}{\omega}. \quad (\text{S3})$$

$$\epsilon_1(\omega) = 1 - \frac{\omega_P^2}{\omega^2 + \gamma^2} = 1 - \frac{\omega_P^2 \tau^2}{1 + \omega^2 \tau^2} \quad (\text{S4})$$

and

$$\epsilon_2(\omega) = \frac{\omega_P^2}{\omega^2 + \gamma^2} \times \frac{\gamma}{\omega} = [1 - \epsilon_1(\omega)] \times \frac{\gamma}{\omega} = \frac{\omega_P^2 \tau^2}{1 + \omega^2 \tau^2} \times \frac{1}{\omega \tau}, \quad (\text{S5})$$

where $\tau = 1/\gamma$ is the *unrenormalized* scattering time.

In the limit of high frequencies (but below the onset of optical interband transitions) and low scattering, $\omega\tau \gg 1$, we find

$$\epsilon_1(\omega) \approx 1 - \frac{\omega_P^2}{\omega^2} \quad \text{and} \quad \epsilon_2 \approx \frac{\omega_P^2}{\omega^2} \times \frac{1}{\omega\tau} \approx 0. \quad (\text{S6})$$

One can therefore plot $\epsilon_1(\omega)$ versus ω^{-2} , which yields $-\omega_P^2$ as the slope. Similarly, plotting $\epsilon(\omega)\omega$ versus ω^{-2} yields $\omega_P^2\gamma$ as the slope.

Sievers²³ writes the result (S5) as

$$\frac{1}{\omega\tau} = \frac{\epsilon_2(\omega)}{1 - \epsilon_1(\omega)} \quad \text{or} \quad \epsilon_1(\omega) = 1 - \tau\omega\epsilon_2(\omega). \quad (\text{S7})$$

Plotting $\epsilon_1(\omega)$ versus $\omega\epsilon_2(\omega)$ therefore yields the scattering time $-\tau$ as the slope.

B. Drude optical conductivity

The complex optical conductivity is defined as

$$\sigma(\omega) = -i\epsilon_0\omega[\epsilon(\omega) - 1] \quad (\text{S8})$$

or written in components as

$$\sigma(\omega) = \sigma_1(\omega) + i\sigma_2(\omega) \quad (\text{S9})$$

with

$$\sigma_1(\omega) = \epsilon_0\omega\epsilon_2(\omega) \quad \text{and} \quad \sigma_2(\omega) = \epsilon_0\omega[1 - \epsilon_1(\omega)]. \quad (\text{S10})$$

Sievers' result (S7) for the Drude scattering rate can also be written in terms of the optical conductivity as

$$\frac{1}{\omega\tau} = \frac{\sigma_1(\omega)}{\sigma_2(\omega)}. \quad (\text{S11})$$

One can therefore determine the scattering rate directly at each frequency, if both real and imaginary parts of the optical conductivity are known, for example from an ellipsometry measurement.

Within the Drude model (S1), the optical conductivity (S8) becomes

$$\sigma(\omega) = \frac{\epsilon_0\omega_P^2}{\gamma - i\omega} = \frac{\epsilon_0\omega_P^2\tau}{1 - i\omega\tau} = \frac{ne^2\tau}{m(1 - i\omega\tau)}. \quad (\text{S12})$$

This can be written in components as

$$\sigma_1 = \frac{\epsilon_0\omega_P^2\gamma}{\omega^2 + \gamma^2} = \frac{\epsilon_0 E_P^2 \Gamma}{\hbar(E^2 + \Gamma^2)}, \quad (\text{S13})$$

$$\sigma_2 = \frac{\epsilon_0\omega_P^2\omega}{\omega^2 + \gamma^2} = \frac{\epsilon_0 E_P^2 E}{\hbar(E^2 + \Gamma^2)}, \quad (\text{S14})$$

$$|\sigma|^2 = \frac{\epsilon_0^2 \omega_P^4}{\omega^2 + \gamma^2} = \frac{\epsilon_0^2 E_P^4}{\hbar^2 (E^2 + \Gamma^2)}. \quad (\text{S15})$$

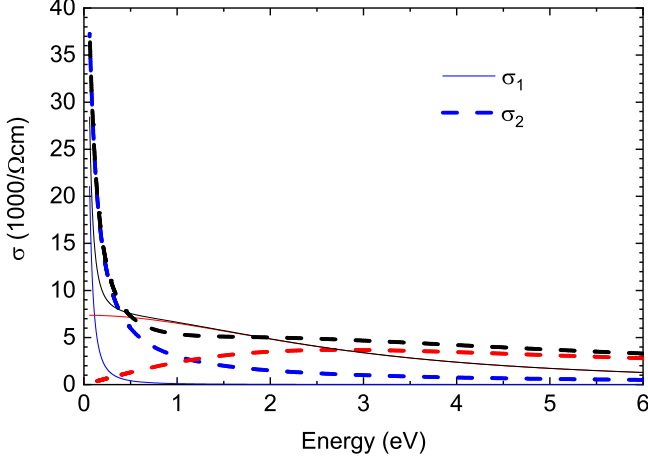


FIG. S6. Real (solid) and imaginary (dashed) parts of the optical conductivity calculated from the Drude model, see Eqs. (S13) and (S14). Drude1 (red): $E_P=12.3$ eV, $\Gamma=2.76$ eV; Drude2 (blue): $E_P=4.73$ eV, $\Gamma=34.6$ meV. The black line shows the sum of both contributions.

We note that

$$\sigma_1(\omega=0) = \frac{\epsilon_0 E_P^2}{\hbar \Gamma} = \sigma_0 \quad \text{and} \quad \sigma_2(\omega=0) = 0. \quad (\text{S16})$$

The real and imaginary parts σ become equal at $\omega=\gamma$.

Figure S6 shows the real and imaginary parts of the optical conductivity calculated from two sets of parameters similar to those labeled Drude1 and Drude2 in Table I. We calculate $\sigma_0=6640/\Omega\text{cm}$ for Drude1 and $\sigma_0=75,500/\Omega\text{cm}$ for Drude2. We therefore associate the Drude1 term with d-electrons (because of their large scattering rate) and the Drude2 term with sp-electrons (because of their dominant contribution to the DC conductivity, see Mott 1936). The total conductivity calculated from our optical data is $82,100/\Omega\text{cm}$, which is lower than, but of the same order of magnitude as the commonly cited electric conductivity of Ni of $146,000/\Omega\text{cm}$. σ_2 indeed becomes 0 at low frequencies for the Drude1 term, but we cannot observe this for the Drude2 term because we did not measure at sufficiently low energies (below $\Gamma=42.1$ meV).

There is a crossing of σ_1 and σ_2 at $\Gamma=2.76$ eV for the Drude1 term. This crossing is below our spectral range for the Drude2 term. At the lowest frequencies, the Drude2 term is the dominant contribution to σ_1 , while the Drude1 term dominates above 1 eV.

Equation (S12) implies

$$\tau^{-1} = \gamma = \frac{\epsilon_0 \omega_P^2}{\sigma} + i\omega = \frac{\epsilon_0 E_P^2 \sigma_1}{\hbar^2 |\sigma|^2} + i \left(\omega - \frac{\epsilon_0 E_P^2 \sigma_2}{\hbar^2 |\sigma|^2} \right) \quad (\text{S17})$$

$$\tau^{-1} = \gamma = \frac{\epsilon_0 \omega_P^2 \sigma_1}{|\sigma|^2} + i\omega \left(1 - \frac{\epsilon_0 \omega_P^2 \sigma_2}{\omega |\sigma|^2} \right), \quad (\text{S18})$$

where we have introduced $E_P = \hbar \omega_P$. We also note that $\epsilon_0/\hbar=134.52$ $1/\Omega\text{cm eV}$ and $\hbar^2 e^2/\epsilon_0 m_0=1.379 \times 10^{-21}$ $\text{cm}^3 \text{eV}^2$. In Gaussian units, $1/\Omega\text{cm}$ is equivalent to $10^{-11}/\text{s}$. Equation (S18) allows us to calculate the unrenormalized scattering rate from the measured optical conductivity, if we “guess” the plasma frequency or determine it from other sources.

C. Renormalized frequency-dependent scattering rate, plasma frequency, and effective mass

Following Sulewski *et al.*,²⁴ we define in MKSA units

$$\Gamma_1(\omega) = \frac{\epsilon_0 E_P^2 \sigma_1}{\hbar |\sigma|^2}, \quad (\text{S19})$$

$$1 + \lambda(\omega) = \frac{\epsilon_0 E_P^2 \sigma_2}{\hbar E |\sigma|^2}, \quad (\text{S20})$$

$$\hbar \gamma^*(\omega) = \frac{\hbar}{\tau^*(\omega)} = \frac{\Gamma_1(\omega)}{1 + \lambda(\omega)}, \quad (\text{S21})$$

$$\omega_P^{*2}(\omega) = \frac{\omega_P^2}{1 + \lambda(\omega)}, \quad \text{and} \quad (\text{S22})$$

$$m^*(\omega) = m [1 + \lambda(\omega)], \quad (\text{S23})$$

which makes Eq. (S18) equivalent to

$$\hbar \tau^{-1} = \hbar \gamma = \Gamma_1(\omega) - i E \lambda(\omega). \quad (\text{S24})$$

Sievers²³ writes Eq. (S22) in terms of the dielectric function $\epsilon(\omega)$ as

$$\frac{E_P^{*2}(\omega)}{E^2} = \frac{\epsilon_2^2(\omega) + [1 - \epsilon_1(\omega)]^2}{1 - \epsilon_1(\omega)} \quad (\text{S25})$$

which is, of course, equivalent.

The unstarred quantities τ , γ , ω_P , and m are the *unrenormalized* scattering time, scattering rate, plasma frequency and the *bare optical band* mass. The equivalent quantities with the asterisk are called the frequency-dependent *renormalized* quantities. m^* is also called the infrared (experimental) mass,²³ if it is calculated using Eq. (S23) from the measured optical conductivity. The quantity $1 + \lambda(\omega)$ is the frequency-dependent *mass enhancement factor*. We have defined Γ_1 in units of energy with an \hbar prefactor. All equations are in MKSA units.

If the optical conductivity $\sigma(\omega)$ follows the Drude model, then it is easy to see from Eq. (S11) that

$$\gamma^*(\omega) = \frac{1}{\tau^*(\omega)} = \frac{\sigma_1}{\sigma_2} \omega = \frac{1}{\tau} \quad (\text{S26})$$

and $1 + \lambda(\omega) = 1$. Therefore, the renormalized plasma frequency is equal to the unrenormalized plasma frequency and the renormalized mass is equal to the bare optical band mass.

It gets more interesting, if the optical conductivity does not show pure Drude behavior, for example because the (classical) frictional force is not proportional to the

velocity (which was one of the assumptions in deriving the Drude and Lorentz models). In a quasi-particle picture, free electrons might interact with other excitations (phonons or interband transitions or surface plasmons²³), which causes deviations of the optical conductivity from the pure Drude response. This is sometimes called the Holstein (1954, 1964) effect. In such cases, we can still calculate the renormalized frequency-dependent scattering rate, because the plasma frequency cancels in Eq. (S21). We can only calculate the renormalized frequency-dependent mass, if the plasma frequency is known (at least approximately). Sometimes, we will guess a value of the plasma frequency in this calculation. An error introduced by an incorrect plasma frequency will only cause a constant factor in the renormalized mass m^* .

D. Application to Drude model with two carrier species

While the frequency-dependent scattering formalism has been applied to a variety of materials,^{23,24,26–30} especially alkali metals, heavy Fermion compounds, and conducting metal oxides, we are not aware of an application of this concept to a dielectric function determined by two species of free carriers. Drude (1900) already speculated that metals required two different species of free charge carriers to explain their optical constants. This topic was revisited by Roberts (1955, 1959) and applied to Ni.

For a single Drude carrier species, the mass enhancement factor equals unity, as already mentioned. The dotted line in Fig. S7 (a) shows the mass enhancement factor calculated with Eq. (S20) from an optical conductivity written as a sum of two free carrier terms¹⁸ given in Eq. (S12). This calculation requires choosing a fixed value of the plasma frequency, so we picked $E_P=4.73$ eV similar to Table I. At first, it seems strange that the renormalized mass parameter would drop from 80% of the bare mass to 13% as the photon energy increases. Since the free carrier absorption is dominated by s-electrons (with a small mass) at low energies and by d-electrons (with a large mass) at high energies, the opposite should be the case. The key to understand this graph is to consider that we used a fixed plasma energy of $E_P=4.73$ eV in this calculation.

It is more helpful to plot the energy dependence of the inverse mass enhancement factor, see the dotted line in Fig. S7 (b). This equals the square of the ratio of the energy-dependent plasma frequency to our assumed value of $E_P=4.73$ eV. For low photon energies, free carrier absorption is dominated by the sp-electrons (term Drude2) with a plasma frequency of $E_P=4.73$ eV, equal to our assumed value. Therefore, the inverse mass enhancement factor is about 1. As the photon energy increases, the contribution to the free carrier absorption by the sp-electrons decreases and the contribution of the d-electrons (Drude1 term) with a plasma frequency of 12.3 eV increases. We therefore expect the inverse mass

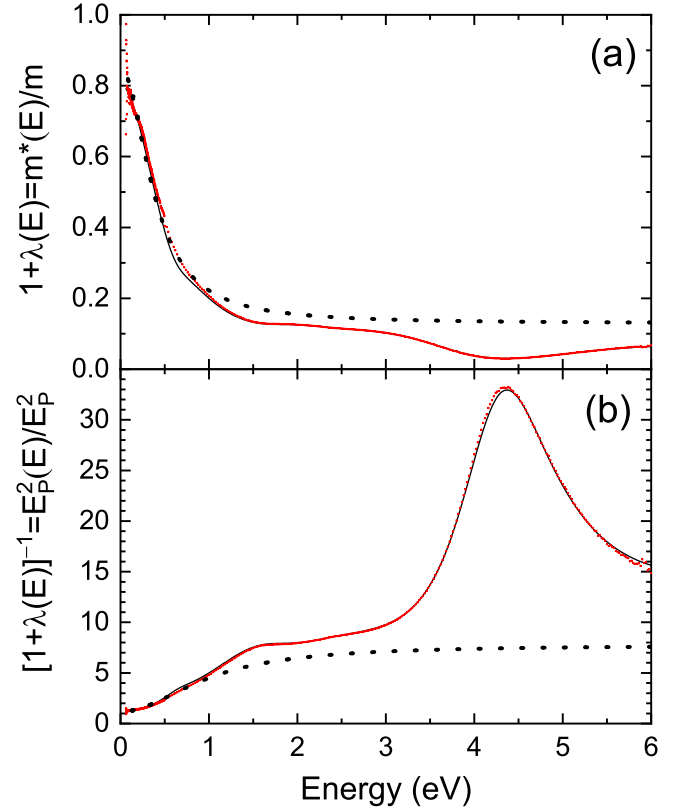


FIG. S7. Mass enhancement factor $1+\lambda(E)$ (a) and its inverse (b) as a function of photon energy, calculated from Eq. (S20). The dotted line shows results calculated from a Drude model with two carrier species as shown in Fig. S6. The symbols and solid lines show results calculated from our experimental data and our product model, respectively. We assumed a value of $E_P=4.73$ eV for the plasma frequency in this figure.

enhancement factor to reach 6.8 at very high energies, which is close to the value of 7.6 at 6 eV, see Fig. S7 (b). The plasma frequency (S2) $\omega_P^2=ne^2/\epsilon_0m$ is determined by the ratio of two parameters, the carrier density and the effective mass. While we expect the effective mass to be larger for d-electrons than for sp-electrons (which tends to decrease the plasma frequency), the carrier density increases even more than the effective mass and therefore the plasma frequency for d-electrons is larger than for sp-electrons,

We now understand why $m^*(E)$ decreases with photon energy. m^* is close to unity at low frequencies, because we have chosen the correct plasma frequency of sp-electrons (4.73 eV) in this frequency range. At higher energies (above 1 eV), the contribution from d-electrons with a plasma frequency of 12.3 eV dominates. The effective mass parameter therefore decreases, because we have chosen a plasma frequency which is much too low for the spectral range above 1 eV. (The same decrease of m^* with increasing energy would occur, if we had chosen $E_P=12.3$ eV in our calculation, but it would reach a high-energy limit of unity.)

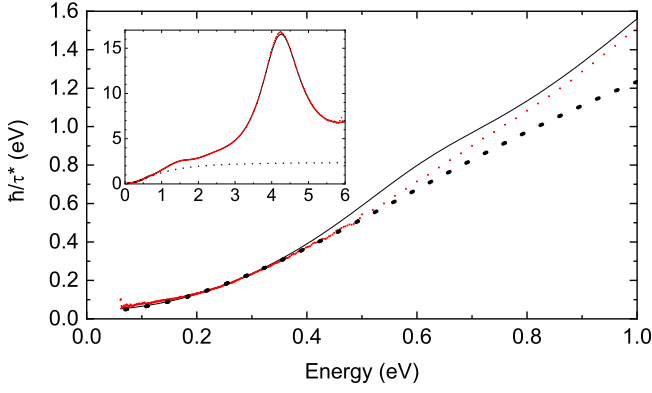


FIG. S8. Frequency-dependent scattering rate as a function of photon energy, calculated from Eq. (S21). The dotted line shows results calculated from a Drude model with two carrier species as shown in Fig. S6. The symbols and solid lines show results calculated from our experimental data and our product model, respectively.

In summary, it is our impression that a frequency-dependent mass parameter is not a useful concept in the description of the optical constants of a free electron gas with two types of carrier with different densities and optical band masses. Instead, it is more intuitive to consider the frequency dependence of the renormalized plasma frequency, see Fig. S7 (b).

The frequency-dependent renormalized scattering rate \hbar/τ^* calculated from a sum of two Drude terms with parameters in Table I is shown in Fig. S8 (dotted). At low energies, \hbar/τ^* equals 0.05 eV, because most of the scattering is due to sp-electrons with a scattering rate of 0.0421 eV. Only a small contribution to the scattering rate is due to d-electrons (and therefore the total value of \hbar/τ^* slightly larger than 0.0421 eV). As the photon energy increases and scattering of d-electrons becomes dominant, \hbar/τ^* increases also, first quadratically and then linearly. The increase flattens out above 1 eV and \hbar/τ^* approaches 2.4 eV at an energy of 2 eV, close to the Drude1 scattering rate of d-electrons shown in Table I.

S4. IMPEDANCE AND REFRACTIVE INDEX

Faraday's Law (the third Maxwell equation) for electromagnetic waves in vacuum reads in MKSA units

$$\vec{\nabla} \times \vec{E} = -\mu_0 \frac{\partial \vec{H}}{\partial t}, \quad (\text{S27})$$

where \vec{E} and \vec{H} are the electric and magnetic field strengths and μ_0 the permeability of free space. For a plane wave with wave vector \vec{k} and angular frequency ω , this becomes

$$\vec{k} \times \vec{E}_0 = \omega \mu_0 \vec{H}_0, \quad (\text{S28})$$

where the subscript 0 stands for the complex amplitude of the plane wave. We can eliminate \vec{k} with the wave

equation

$$\vec{\nabla}^2 \vec{E} - \frac{1}{c^2} \frac{\partial^2 \vec{E}}{\partial t^2} = 0 \quad (\text{S29})$$

and the resulting dispersion equation

$$k^2 = \frac{\omega^2}{c^2}. \quad (\text{S30})$$

From Eqs. (S28) and (S30), we find the relationship

$$E_0 = \mu_0 c H_0 = \sqrt{\frac{\mu_0}{\epsilon_0}} H_0 = Z_0 H_0 \quad (\text{S31})$$

between the magnitudes of the electric and magnetic field strength amplitudes, where we have introduced the speed of light in vacuum

$$c = \frac{1}{\sqrt{\epsilon_0 \mu_0}} \quad (\text{S32})$$

and the impedance of vacuum

$$Z_0 = \sqrt{\frac{\mu_0}{\epsilon_0}} = 377 \, \Omega. \quad (\text{S33})$$

The corresponding Maxwell equation (Faraday's Law) in a dispersive medium (e.g., a metal) is

$$\vec{\nabla} \times \vec{E} = -\frac{\partial \vec{B}}{\partial t}, \quad (\text{S34})$$

where $\vec{B} = \mu \mu_0 \vec{H}$ is the magnetic flux density, or

$$\vec{k} \times \vec{E}_0 = \omega \vec{B}_0 = \omega \mu \mu_0 \vec{H}_0 \quad (\text{S35})$$

for plane waves. At optical frequencies, $\mu=1$. In an anisotropic medium, we no longer have a wave equation similar to Eq. (S29) (because \vec{E} is not in general perpendicular to the wave vector). We therefore restrict the following discussions to isotropic media.

The wave equation

$$\vec{\nabla}^2 \vec{E} - \frac{1}{c^2} \frac{\partial^2 \epsilon \vec{E}}{\partial t^2} = 0 \quad (\text{S36})$$

for an isotropic medium with $\mu=1$ results in the dispersion relation

$$|k|^2 = \epsilon \frac{\omega^2}{c^2} \quad (\text{S37})$$

for a generalized (or inhomogeneous) plane wave with a complex wave vector \vec{k} and real angular frequency ω (Mansuripour 1995, Stratton 2007). From Eqs. (S35) and (S37), we find the relationship

$$\sqrt{\epsilon} E_0 = \mu_0 c H_0 = \sqrt{\frac{\mu_0}{\epsilon_0}} H_0 = Z_0 H_0 \quad (\text{S38})$$

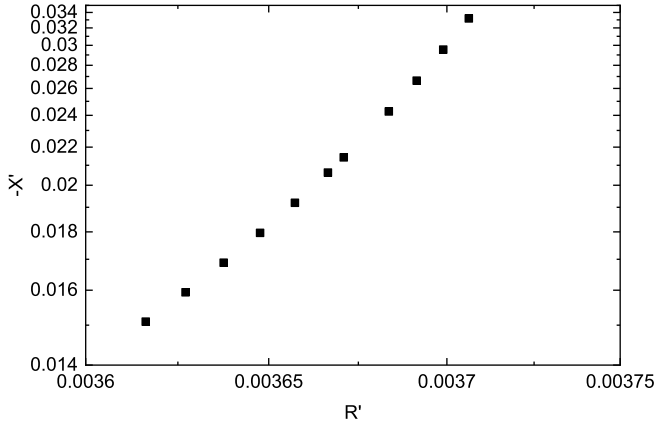


FIG. S9. Lenham-Treherne diagram⁹ for the complex impedance (in units of Z_0) at selected wavelengths between 8 and 17 μm calculated from a Drude dielectric function with $E_P=4.7$ eV and a Drude broadening $\Gamma=35$ meV. Note the reciprocal axes.

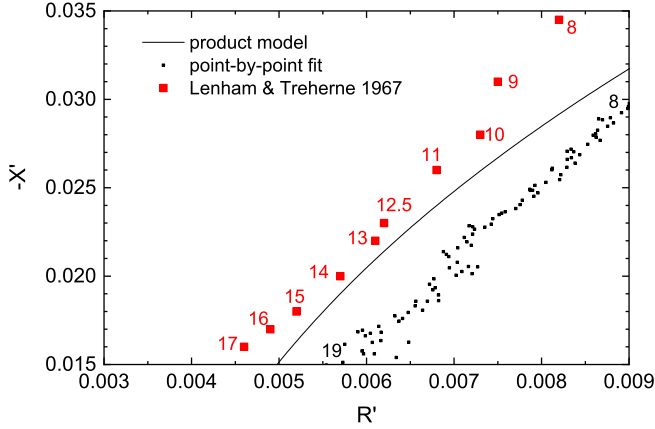


FIG. S10. Argand diagram of the complex optical impedance (in units of Z_0) defined in Eqs. (S41) and (S42) calculated from the complex dielectric function shown in Fig. 3 for polycrystalline Ni at 300 K. Note the linear axes. Small symbols show results from a point-by-point fit. The line was calculated from the product model (5) with parameters in Table II. Large symbols show the results of Lenham and Treherne on Ni single crystals from 8 to 17 μm wavelength,¹⁰ indicated by numbers.

between the magnitudes of the amplitudes of the electric and magnetic field strengths. This is similar to Eq. (S31) except for a factor $\sqrt{\epsilon}$, where ϵ is the frequency-dependent dielectric constant. This results in

$$E_0 = \frac{Z_0}{\sqrt{\epsilon}} H_0 = Z H_0, \quad (\text{S39})$$

where $Z = Z_0/\sqrt{\epsilon} = R + iX$ is the complex impedance of the wave in an isotropic medium with $\mu=1$. R and X are the real part (resistance) and imaginary part (reactance) of the complex impedance.¹⁰ It is convenient to introduce

the dimensionless complex impedance¹⁰

$$Z' = R' + iX' = \frac{Z}{Z_0} = \frac{1}{\sqrt{\epsilon}} = \frac{1}{n + i\kappa} \quad (\text{S40})$$

with real part

$$R' = \frac{n}{n^2 + \kappa^2} \quad (\text{S41})$$

and imaginary part

$$X' = \frac{-\kappa}{n^2 + \kappa^2}. \quad (\text{S42})$$

The older literature¹⁰ sometimes includes a factor of $4\pi/c$, which arises from the definition of the surface impedance of a conductor (Dingle 1953, Jackson 1975) in Gaussian units. This does not affect the definition of the dimensionless impedance Z' in Eq. (S40). Our results are therefore directly comparable to those of Lenham and Treherne.¹⁰

It was customary in the older literature¹⁰ to plot X' (reactance) versus R' (resistance), in units of Z_0 , sometimes with reciprocal axes.⁹ It is not possible to write the complex refractive index with real part (Fox 2010)

$$n = \frac{1}{\sqrt{2}} \sqrt{\epsilon_1 + \sqrt{\epsilon_1^2 + \epsilon_2^2}} \quad (\text{S43})$$

and imaginary part

$$\kappa = \frac{1}{\sqrt{2}} \sqrt{-\epsilon_1 + \sqrt{\epsilon_1^2 + \epsilon_2^2}} \quad (\text{S44})$$

for free-carrier absorption with simple equations, without approximations that are too restrictive ($\omega\tau \gg 1$) for our purposes. We therefore show $-X'$ versus R' with reciprocal axes for a Drude metal with plasma frequency 4.7 eV (carrier density $n=1.6 \times 10^{22}$ cm^{-3}) and a Drude broadening of 35 meV, which corresponds to a scattering time $\tau=19$ fs (similar to Ni, see Table I) in Fig. S9. The negative sign in $-X'$ is due to our convention $\exp(-i\omega t)$ for the time-varying fields. This figure is similar to Fig. 1 in Ref. 9.

From our dielectric function for polycrystalline Ni at 300 K (determined from a point-by-point fit and from our product model), we can calculate the complex impedance. The results are shown in Fig. S10. As mentioned by Lenham and Treherne,⁹ an Argand diagram for the complex impedance is much more sensitive to show small differences between data and a model than the dielectric function (Fig. 3) or the complex optical conductivity (Fig. 4). We compare our results with those measured by Lenham and Treherne¹⁰ in Fig. S10. The agreement between our data and theirs is about the same as the agreement between our data and our product model. A horizontal shift of the Argand impedance curve towards smaller R' values indicates a larger scattering time.⁹ In other words, the resistance in the Lenham-Treherne single crystals¹⁰ should be expected to be smaller than in our polycrystalline Ni samples.

55. ANOMALOUS SKIN EFFECT

The anomalous skin effect¹ (Dingle 1953, Wooten 1972, Jones 1972) affects the optical response of metal surfaces when the electron mean free path $l=v_F\tau$ (where v_F is the Fermi velocity) becomes of the order of the penetration depth or larger. We calculate $l=16$ nm from $v_F=10^8$ cm/s, see Ref. 32, and $\tau=\hbar/\Gamma=16$ fs (Table I). Our penetration depths are at least 75 nm, i.e., much larger than the electron mean free path, see Fig. S4. We therefore do not take the anomalous skin effect into account in the analysis of our room temperature data. (We were unable to confirm the value of v_F given by Kamini *et al.*¹³ in the sources they cited.)

According to Lynch and Hunter,¹ the anomalous skin effect correction to the normal-incidence reflectance is $\frac{3}{4}\frac{v_F}{c}$ for diffuse surface scattering, which equals 0.0025 for Ni.

The question about the anomalous skin effect contributions to ellipsometry data should be revisited with low-temperature measurements of a high-conductivity metal like Au or Al.

Brückner *et al.* (1989) write that the complex refractive index must sometimes be modified due to the anomalous skin effect. An ellipsometry or reflectance experiment measures an effective complex refractive index $n^* + i\kappa^*$, which is related to the Drude-Lorentz refractive index $n + i\kappa$ by

$$\frac{n^* + i\kappa^*}{n + i\kappa} = 1 - \frac{3v_F}{16c} \frac{\kappa - in}{-i + (1/\omega\tau)}. \quad (\text{S45})$$

Shelton *et al.* (2008) take the viewpoint that the free carrier concentration n in the Drude model must be replaced with a frequency-dependent carrier concentration

$$n^*(\omega) = \frac{n}{\tau} \frac{\beta^{2/3}}{v_F^{2/3}} \sqrt[3]{\frac{2m}{\omega n e^2 \mu_0}}. \quad (\text{S46})$$

The dimensionless parameter β is related to the surface roughness and describes if scattering of electrons by the surface is specular or diffuse.

56. ZEROS AND POLES ON THE IMAGINARY AXIS

It is well known^{18,25} (Berreman 1968) that the dielectric function of a solid can be written as a product (5) with zeros and poles in the complex plane. In the case of infrared lattice absorption, the poles represent the transverse optical phonons and the zeros the longitudinal optical phonons. For electronic transitions, the poles represent the energy gap (resonance frequency) and the zeros the strengths of the transitions.¹⁸ For a metal, the free carrier absorption is described by a pole on the imaginary axis, where the associated zero (which represents the plasma frequency) is not on the imaginary axis.

We struggled for some time with how to model the dielectric function of a metal using Eq. (5) if the free

TABLE SI. The optical constants of a metal calculated from a sum of two Drude terms in Eq. (2) (top part) were fitted with a product of two Drude terms as in Eq. (5) (bottom part).

	$\hbar\omega_P$ (eV)		$\hbar\gamma$ (eV)	
Drude 1	11.9		2.87	
Drude 2	4.86		0.0421	
	$\hbar\omega_0$ (eV)	$\hbar\gamma_0$ (eV)	$\hbar\omega_L$ (eV)	$\hbar\gamma_L$ (eV)
Drude 1	0	2.87	12.8	2.46
Drude 2	0	0.0422	0	0.450

carrier absorption is described by two species of carriers. We solved this problem numerically and found an equivalent description of the dielectric function as a sum or a product of Drude oscillators with parameters listed in Table SI. The results are somewhat surprising and warrant some discussion. We find that the Drude parameters of the term with the larger plasma frequency (Drude 1) are comparable in both models. The broadenings are identical and the plasma frequency differs by only 10%. The broadenings of the second Drude term are also identical. It is surprising, however, that the zero of the second Drude term is on the imaginary axis. This is the first time we have encountered the need for a zero of the dielectric function on the imaginary axis.

57. OPTICAL CONSTANTS OF GOLD

A. Ellipsometric angles and model parameters

For comparison with Ni, we also measured the ellipsometric angles for gold using the same instruments, but in air with angles of incidence from 65° to 80° with 5° steps. The gold layer used for these measurements was a calibration standard (gold mirror) shipped with the FTIR ellipsometer by the J. A. Woollam Company. This gold layer was not cleaned (by heating in UHV) and measured in air. Therefore, this sample was probably not clean, but covered with surface layers. Therefore, we consider the optical constants reported here a qualitative estimate. They do not carry the same accuracy as our Ni data. The main reason for reporting optical constants of gold in this context is to have a qualitative comparison of the physics governing the optical constants of these two materials. Using x-ray reflectance, we estimate the surface roughness of the gold mirror to be about 3 nm.

The ellipsometric angles of gold acquired at four angles of incidence (65° to 80° with 5° steps) are shown in Fig. S11. We see that the reststrahlen band in gold is much more pronounced than in Ni. For gold, ψ stays just below 45° to about 2 eV. For Ni, ψ drops below 45° at very low energies, because of d-intraband transitions. (Within a reststrahlen band, where ψ is nearly 45°, ellipsometry is very sensitive to weak absorption processes, see Willett-Gies, 2015.) Since Au is a noble metal, the d-bands are

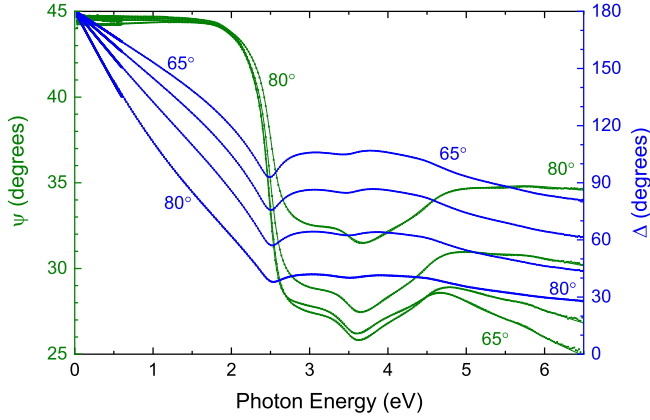


FIG. S11. Ellipsometric angles ψ and Δ for a gold mirror measured in air as a function of photon energy from 65° to 80° angle of incidence.

completely full and such d-intraband transitions are not possible.

The deviation of ψ from 45° is measurable and increases with angle of incidence (0.3° for 65° incidence angle, 0.6° at 80°). It is related to the Drude scattering rate. We observe a small discontinuity in our ψ data at 1.2 eV, where the VASE ellipsometer switches detectors. The ellipsometric angle Δ decreases almost linearly from 180° with increasing photon energy. At our low-energy end of the spectral range (0.03 eV), Δ is still a few degrees lower than 180° , especially for shallow incidence angles. The deviation of Δ from 180° is not related to the Drude scattering rate. Instead, the slope of Δ is related to the plasma frequency. At zero energy, all Δ curves converge to 180° like a fan.

The ellipsometric angle ψ drops sharply at 2.5 eV due to the onset of interband transitions. We model this transition with a Tauc-Lorentz oscillator centered at 2.54 eV. The asymmetry of this oscillator, with a sharp cutoff at the Tauc gap of 2.34 eV and a broadening of 0.47 eV shapes the knee of ψ between 1.8 and 2.3 eV. Depending on the angle of incidence, Δ has a more or less pronounced minimum at this transition. We added six Gaussians and a pole to model the dispersion and achieved an excellent fit to the data in Fig. S11, with the parameters listed in Table SII. (We chose Gaussians rather than Lorentzians to avoid the slow drop of the Lorentzians, which might influence the absorption at low energies.) The strongest Gaussians at 3.1 and 4.2 eV lead to valleys in ψ and Δ .

B. Optical constants

The pseudo-dielectric function of gold, determined from the ellipsometric angles with a point by point fit (ignoring surface overlayers) and from the model with parameters listed in Table SII, is shown in Fig. S12. The Drude divergence is much stronger in gold than in nickel,

TABLE SII. Parameters used to describe the optical constants of polycrystalline gold with a sum of oscillators: Energy E , Tauc gap E_g , plasma frequency $E_P = \hbar\omega_P$, broadening Γ , and the pole amplitude A are in units of eV, the Gaussian amplitudes are dimensionless. All parameters are given with three significant digits. Due to parameter correlations, the uncertainty is probably much larger.

	A	E	Γ	E_g	E_P
Drude			0.0438		8.53
Tauc-Lorentz	61.5	2.54	0.466	2.34	
Gauss 1	3.63	3.08	1.20		
Gauss 2	0.697	3.75	0.479		
Gauss 3	2.82	4.16	1.02		
Gauss 4	0.670	5.013	1.10		
Gauss 5	1.01	5.33	2.33		
Gauss 6	2.68	8.28	7.07		
Pole	21.3	423			

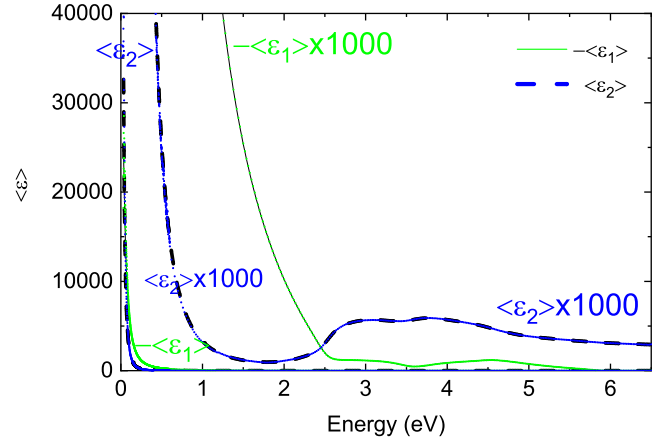


FIG. S12. Pseudodielectric function of a gold mirror (without surface corrections). Symbols show the results of a point-by-point fit, ignoring overlayers, lines show the best fit to the ellipsometric angles using a sum of oscillators with parameters shown in Table SII.

because gold has a very low scattering parameter. In gold, conduction is entirely due to s-electrons (which have a low value of Γ). The d-band conduction (with its large scattering rate) is missing in gold, because all d-bands are filled. Therefore, $\langle \epsilon_2 \rangle$ dips below 1 at 1.8 eV. At higher energies, $\langle \epsilon_2 \rangle$ rises again due to interband transitions. The onset of interband transitions is very sharp and stands well above the low Drude contribution, thus the need for a Tauc-Lorentz oscillator.

The Drude divergence can be removed partially by plotting the optical conductivity, which is shown in Fig. S13. However, for Au the electrical conductivity at low energies is much larger than the interband conductivity above 2 eV. This makes it hard to show the electrical and interband conductivity on the same graph. From our Drude parameters in Table SII, we calculate a DC conductivity of 5×10^6 1/ Ω cm from Eq. (S16), which is an order of magnitude lower than σ_0 derived from electrical measurements. The anomalous skin effect may play

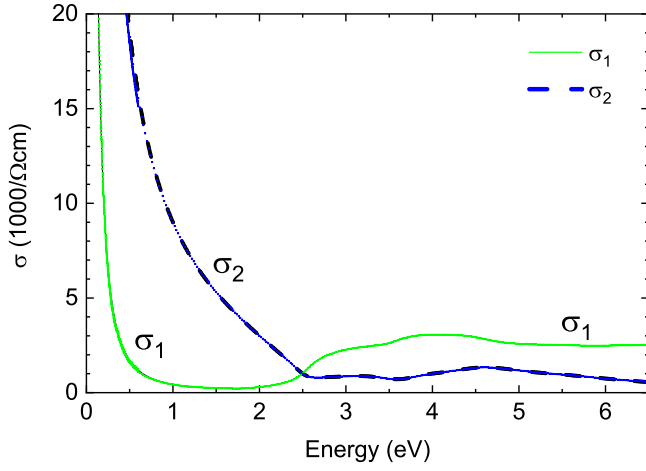


FIG. S13. Same data as in Fig. S12, but shown as an optical pseudo-conductivity.

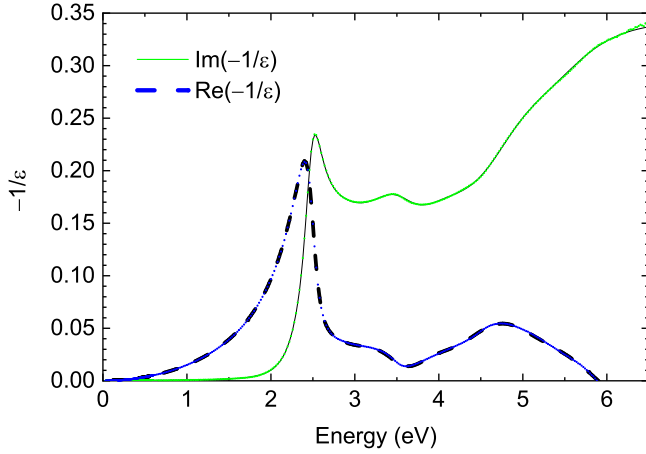


FIG. S14. Same data as in Fig. S12, but shown as a pseudo-loss function.

a role here, since high frequencies reduce the number of carriers contributing to the electronic transport (Shelton 2008).

The loss function for gold (shown in Fig. S14) is dominated by peaks related to interband absorption in the 2 to 4 eV range. At higher photon energies, $\text{Im}(-1/\langle\epsilon\rangle)$ still rises, because the plasma frequency at 8.5 eV is outside of our spectral range. The complex refractive index is shown in Fig. S15. We note that $\langle n \rangle \ll \langle \kappa \rangle$ (Fox 2010). Interband transitions are more obvious in $\langle n \rangle$ than in $\langle \kappa \rangle$. The pseudo-absorption coefficient $\langle \alpha \rangle$ and the pseudo-penetration depth $\langle \lambda_P \rangle$ are shown in Fig. S16. We note that a discontinuity in the data near 0.7 eV, where we have merged data from both ellipsometers. Also, the absorption coefficient is more sensitive to small differences between data and model. The absorption coefficient is small at the longest wavelengths and then rises sharply and reaches a global maximum near 0.3 eV. It then falls gradually and reaches a global minimum

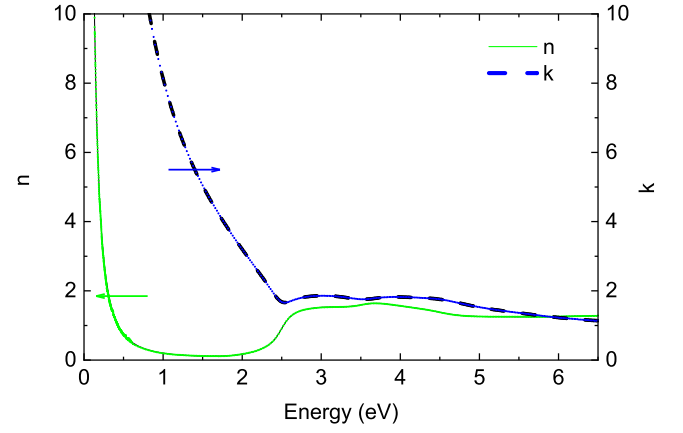


FIG. S15. Same data as in Fig. S12, but shown as a complex pseudo-refractive index $\langle n \rangle + i \langle \kappa \rangle$.

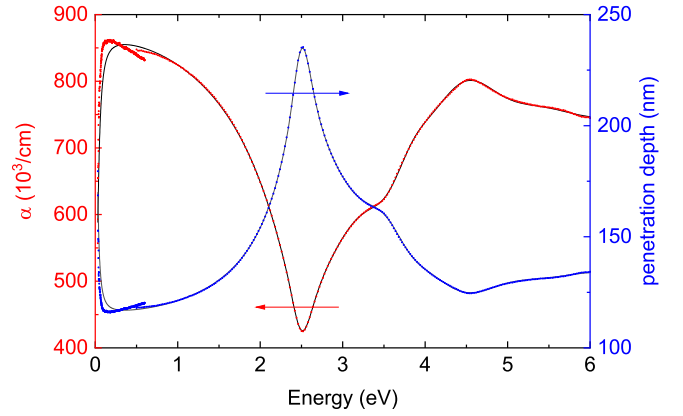


FIG. S16. Same data as in Fig. S12, but shown as a pseudo-absorption coefficient $\langle \alpha \rangle$ and a pseudo-penetration depth $\langle \lambda_P \rangle$.

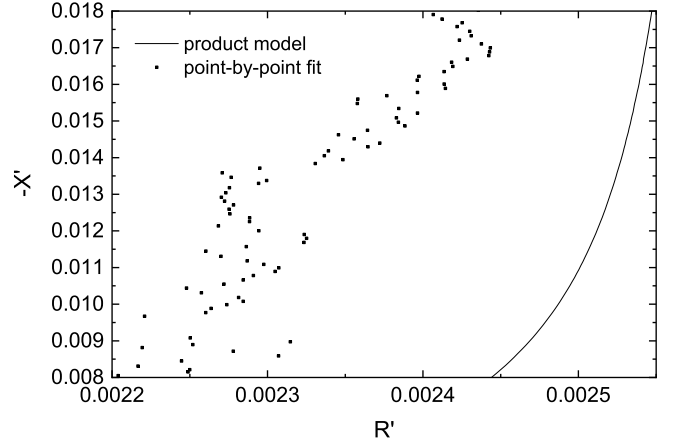


FIG. S17. Argand diagram of the complex optical pseudo-impedance of gold at 300 K (in units of Z_0) defined in Eqs. (S41) and (S42) in the mid-infrared (from 0.07 to 0.16 eV), calculated from the complex pseudo-dielectric function shown in Fig. S12. Small symbols show results from a point-by-point fit. The line was calculated from the Drude-Lorentz model with parameters in Table SII.

near 2.5 eV, just below the onset of interband transitions. As we compare the penetration depth in the mid-infrared between Au and Ni, we notice that the penetration depth is only 125 nm below 1 eV, significantly lower than for Ni due to the absence of d-intraband transitions in Au. This will have consequences for the anomalous skin effect in both materials. The complex optical pseudo-impedance of gold at 300 K (in units of Z_0), defined in Eqs. (S41) and (S42), is shown in Fig. S17 in the mid-infrared spectral region (from 0.07 to 0.16 eV). We note that the resistance of gold is lower than the resistance of Ni, as expected. The reactance also is much smaller for gold. This graph clearly shows the discrepancy between our model and the point-by-point fit results.

C. Drude parameters

To determine the plasma frequency graphically using Eq. (S6), we plot ϵ_1 versus $1/E^2$ in Fig. S18. We find $E_P=8.13$ eV, which is in good agreement with our parameter $E_P=8.53$ in Table SII determined from a Drude-Lorentz fit to the ellipsometric angles. We also plot $\epsilon_2 E$ versus $1/E^2$, which yields $E_P^2 \Gamma=2.7$ eV as the slope, in good agreement with the value of 3.2 eV calculated from the data in Table SII. Overall, this graph seems qualitatively similar for Ni and Au and therefore free carrier absorption should play an important role in both materials.

The frequency-dependent mass parameter $m^*(E) = m[1 + \lambda(E)]$ calculated from Eq. (S20) and its inverse, the frequency-dependent plasma frequency $E_P(E)$ are shown in Fig. S19. In our Drude-Lorentz model (solid line), the mass is constant in the infrared, as expected for transport with a single species of Drude carriers (dotted line). This trend is supported by the data obtained from the point-by-point fit between 0.2 and 0.8 eV (symbols). In the visible, the mass peaks sharply, as interband transitions contribute as well. The initial rise of the mass below 0.2 eV is puzzling. In a complementary view, the plasma frequency drops here. This is not supported by our Drude-Lorentz model. Indeed, as we explore the ellipsometric angles in this spectral region, we find that ψ approaches the ideal metallic value of 45° faster than predicted by our Drude-Lorentz model, see Fig. S20. It is not clear if this is an issue with our model parameters, an experimental error in the ellipsometry measurement, or a physics effect, such as the anomalous skin effect or diffraction effects described by Humlíček and Bernhard (2004). This discrepancy requires additional work, for example measurements at low temperatures on a clean Au sample.

The frequency-dependent scattering rate for gold at 300 K, calculated from Eq. (S21), is shown in Fig. S21. It is quite apparent that the scattering rate is nearly independent of energy in the infrared, as expected from the Drude response for an electron gas with a single species of carriers (shown by the dotted line). It increases only

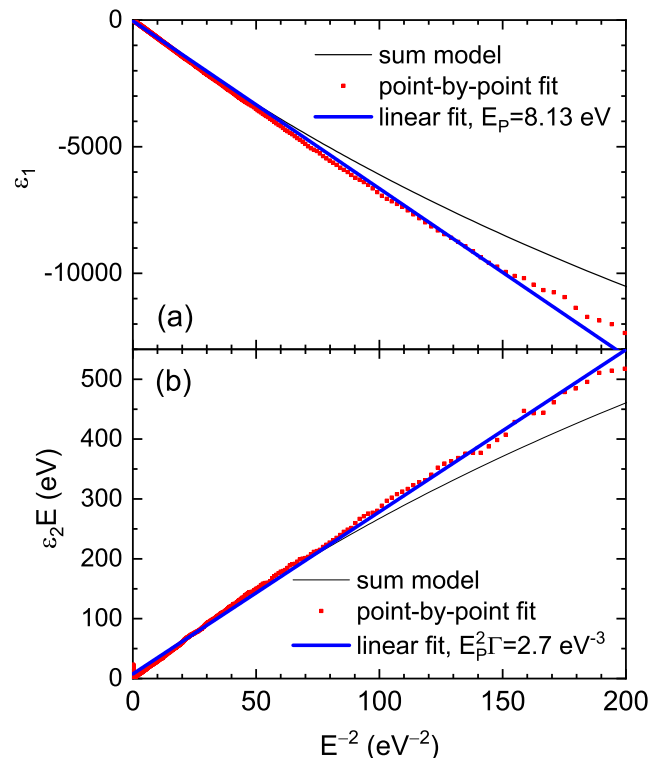


FIG. S18. Same as Fig. 7, but for gold (without surface corrections).

slightly from 0.042 at 0.03 eV to 0.049 eV at 1eV, similar to the Drude scattering rate of 0.044 eV in our Drude-Lorentz model, see Table SII. This slight increase is probably from the tail in our Tauc-Lorentz oscillator due to interband transitions. These interband transitions show a strong rise in the scattering rate in the visible and UV spectral regions. This nearly constant scattering rate for gold is in stark contrast to Ni, see Fig. S8. Conduction from d-electrons in Ni (with a much larger scattering rate) causes a nearly linear rise of \hbar/τ^* . Since the d-bands are full in gold and do not contribute to electronic conduction, there is only one species of Drude carriers and thus a nearly frequency-independent \hbar/τ^* .

ADDITIONAL REFERENCES

- P. Drude, *Zur Ionentheorie der Metalle*, Phys. Z. **1**, 161 (1900).
- N. F. Mott, *The electrical conductivity of transition metals*, Proc. Roy. Soc. Lond. A **153**, 699 (1936).
- J. A. Stratton, *Electromagnetic Theory* (McGraw-Hill, 1941, New York), reprinted by IEEE in 2007.
- T. Holstein, *Optical and infrared volume absorptivity of metals*, Phys. Rev. **96**, 535 (1954).
- S. Roberts, *Interpretation of the optical properties of metal surfaces*, Phys. Rev. **100**, 1667 (1955).
- S. Roberts, *Optical properties of nickel and tungsten and their interpretation according to Drude's formula*,

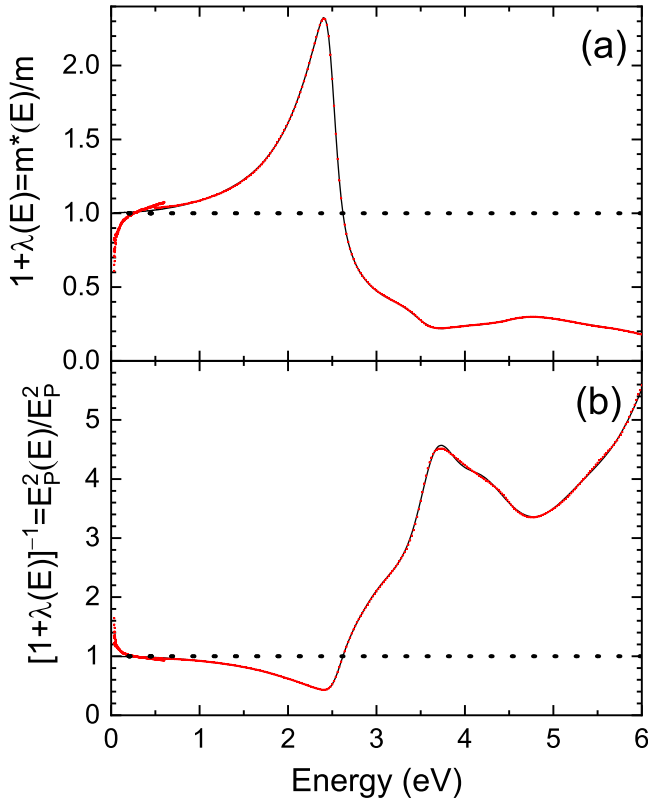


FIG. S19. Mass enhancement factor $1 + \lambda(E)$ (a) and its inverse (b) as a function of photon energy for Au at 300 K, calculated from Eq. (S20). The dotted line shows results calculated from a Drude model with a single carrier species. The symbols and solid lines show results calculated from our experimental data and our Drude-Lorentz model, respectively. We assumed a value of $E_P=8.53$ eV for the plasma frequency in this figure.

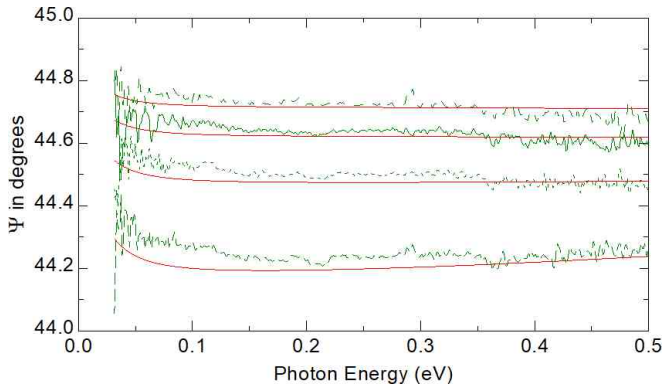


FIG. S20. Ellipsometric angle ψ of gold at 300 K in the infrared. Green and red lines show experimental data and results from a Drude-Lorentz model, respectively. The experimental data approach 45° faster than our model at the lowest energies.

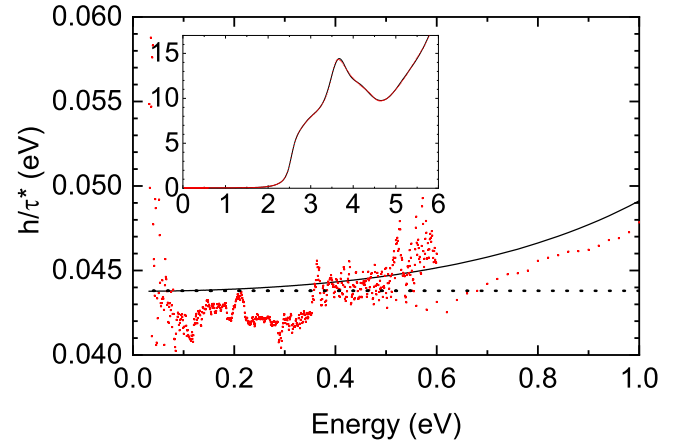


FIG. S21. Frequency-dependent scattering rate as a function of photon energy for gold, calculated from Eq. (S21). The symbols and solid lines show results calculated from our experimental data and our Drude-Lorentz model, respectively. The dotted line shows the Drude response without the Lorentz contributions of interband transitions.

- Phys. Rev. **114**, 104 (1959).
- T. Holstein, *Theory of transport phenomena in an electron-phonon gas*, Ann. Phys. **29**, 410 (1964).
 - R. B. Dingle, *The anomalous skin effect and the reflectivity of metals*, Physica **19**, 311 (1953).
 - D. W. Berreman and F. C. Unterwald, Phys. Rev. **174**, 791 (1968).
 - F. Wooten, *Optical Properties of Solids* (Academic, New York, 1972).
 - M. C. Jones, D. C. Palmer, and C. L. Tien, *Infrared absorptivities of transition metals at room and liquid-helium temperatures*, J. Opt. Soc. Am. **62**, 353 (1972).
 - J. D. Jackson, *Electromagnetic Theory* (Wiley, 1975, New York) 2nd edition.
 - L. J. Hanekamp and A. van Silfhout, *The behaviour of oxygen on Ni (110) investigated by ellipsometry and AES*, J. Phys. Colloques **44**, 469 (1983).
 - M. Brückner, J. H. Schäfer, and J. Uhlenbusch, *Ellipsometric measurement of the optical constants of solid and molten aluminum and copper at $\lambda=10.6 \mu\text{m}$* , J. Appl. Phys. **66**, 1326 (1989).
 - M. Mansuripur, *The Physical Principles of Magneto-optical Recording* (Cambridge University Press, 1998, Cambridge, UK).
 - J. Humlíček and C. Bernhard, *Diffraction Effects in infrared ellipsometry of conducting samples*, Thin Solid Films **455-456**, 177 (2004).
 - D. J. Shelton, T. Sun, J. C. Ginn, K. R. Coffey, and G. D. Boreman, *Relaxation time effects on dynamic conductivity of alloyed metallic thin films in the infrared band*, J. Appl. Phys. **104**, 103514 (2008).
 - M. Fox, *Optical Properties of Solids* (Oxford University Press, 2010, Oxford, UK) 2nd edition.
 - T. I. Willett-Gies, C. M. Nelson, L. S. Abdallah, and S. Zollner, *Two-phonon absorption in LiF and NiO from infrared ellipsometry*, J. Vac. Sci. Technol. A **33**, 061202 (2015).